CHALMERS
UNIVERSITY OF TECHNOLOGY

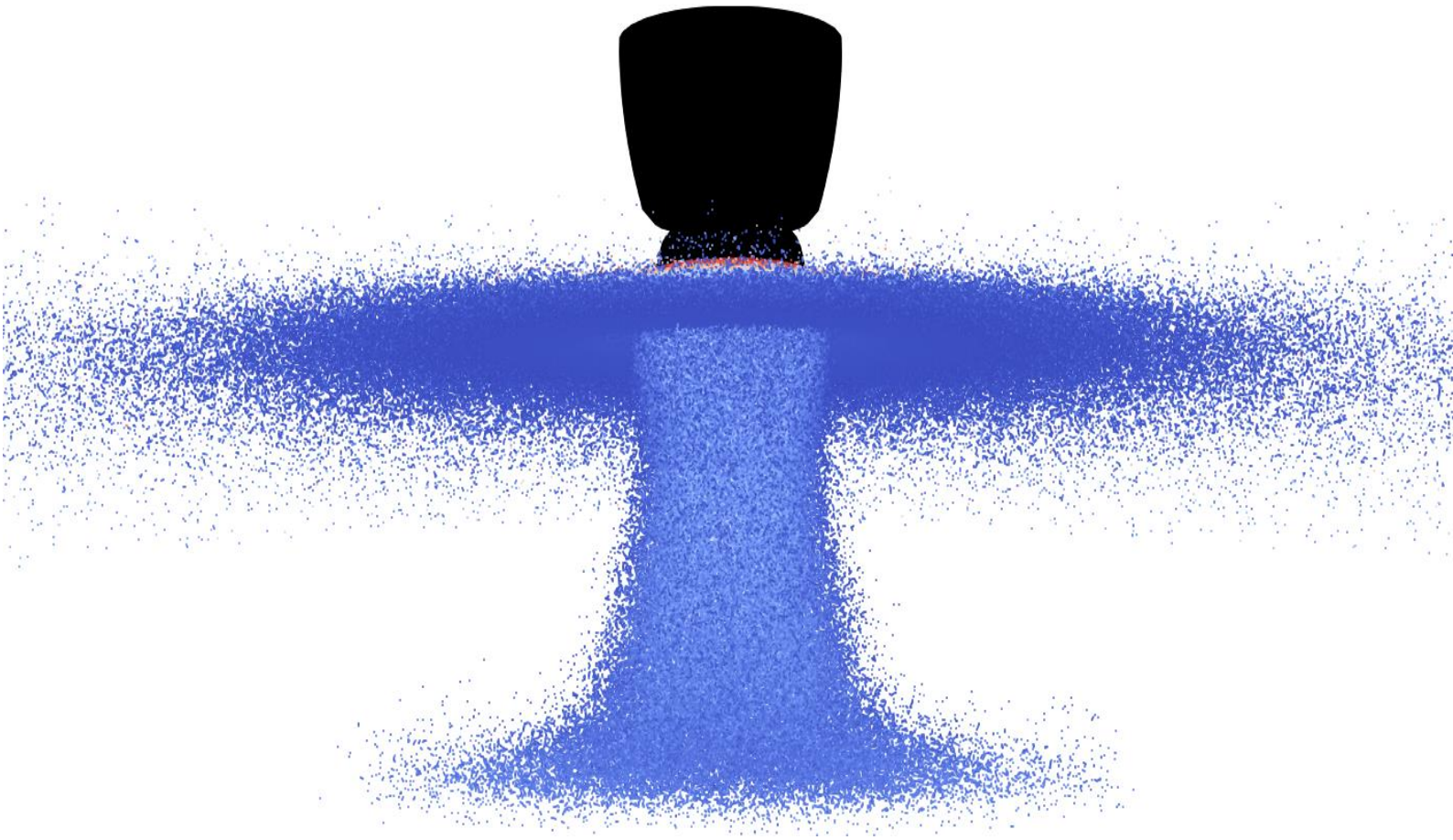

Computationally Efficient Domain Decomposition and Near-Bell Coupling of Rotary Spray Paint Bells

Master's thesis in Applied Mechanics

DAVID ANDERSSON

DEPARTMENT OF MECHANICS AND MARITIME SCIENCES

CHALMERS UNIVERSITY OF TECHNOLOGY
Gothenburg, Sweden 2023
www.chalmers.se

MASTER'S THESIS IN APPLIED MECHANICS

Computationally Efficient Domain Decomposition and Near-Bell Coupling of Rotary Spray Paint Bells

DAVID ANDERSSON

CHALMERS
UNIVERSITY OF TECHNOLOGY

Department of Mechanics and Maritime Sciences
Division of Fluid Dynamics

CHALMERS UNIVERSITY OF TECHNOLOGY
Göteborg, Sweden 2023

Computationally Efficient Domain Decomposition and
Near-Bell Coupling of Rotary Spray Paint Bells

DAVID ANDERSSON

Department of Mechanics and Maritime Sciences
Division of Fluid Dynamics
Fraunhofer Chalmers Centre
Chalmers University of Technology
SE-412 96 Göteborg
Sweden
Telephone: + 46 (0)31-772 1000

Cover:
Snap shot of paint particles simulated in IBOFlow for 0.02 seconds

Printed By Chalmeres Reproservice
Göteborg, Sweden 2023

Computationally Efficient Domain Decomposition and-
Near-Bell Coupling of Rotary Spray Paint Bells
David Andersson
Department of Mechanics and Maritime Sciences
Chalmers University of Technology

Abstract

An industrial spray paint application is a multiscale, multiphysics and multiphase problem requiring large efforts for efficient and accurate modelling. Fraunhofer Chalmers Centre (FCC) has developed the computational tool "IBOFlow" for these purposes, the efficiency of which was the subject of this thesis.

The multiphase aspects combine a strong shaping airflow with the injection of liquid paint or powder which is modelled using an Eulerian-Lagrangian framework with a two-way coupling between the phases. The multiphysics modelled are fluid dynamics, particle dynamics and electrostatic forces which are also coupled with each other. Lastly, and the focus of this thesis, is the modelling of the multiscale issue. The smallest spatial and temporal scales near the paint injection are currently modelled as compressible in a resource demanding process which is separate from the larger scales. The small scales are subsequently imported as a boundary condition on a coarser simulation where both the spatial and temporal scales extend to cover an entire paint job. Different desired finishing results require certain parameter optimizations where a multitude of compressible simulations are needed to model the different settings, referred to as *brushes*. This process quickly becomes both time and resource intensive mainly due to the large optimization spaces.

This thesis has investigated the possibility of an incompressible simplification for the smaller temporal and spatial scales. The incompressible simplification was incrementally tested and validated for larger and larger fractions of the compressible boundary condition with the goal to reduce the number of required compressible simulations to one while also keeping sufficiently good accuracy. It was first tested on a pure airflow and subsequently on a fluid-particle coupled flow. Lastly a cross validation was tested where the imported boundary condition was kept constant as different particle injection parameters varied.

The final result showed that a pure airflow could be simulated incompressibly from $0.5\,cm$ below the injection point and downwards with an error of 2.6% in the high velocity regions. The addition of particles and its two-way coupling on the fluid significantly reduced the errors in the re-circulation region and also resulted in a small improvement in the higher velocity regions. The cross validation showed that a single compressible boundary condition could be used for all injection cases with a maximum error of 2.8% in the high velocity regions and an average error of 2.15%. Larger errors, mostly between 3 and 4%, were obtained in a re-circulation region in the interior flow. Comparing the errors obtained from the airflow fields to corresponding errors in the paint thickness distributions showed that the magnitude of the errors from the airflow field could in several cases approximate how well the thickness distribution turned out. In other cases the results between the different validation methods diverged from each other.

Keywords: CFD, ERBS, Compressible, Incompressible, Immersed Boundary Methods

Acknowledgements

It has been six months since I started with this thesis and while the initial learning curve was steep, I would like to give my deepest gratitude to my supervisor Tomas Johnson as well as Andrea Ruggio for giving me the right tools from the start. For lending their time and having patience. For always being friendly, knowledgeable and helpful.

I would like to thank Fraunhofer Chalmers Centre for hiring me as a contracted student which turned into this thesis and for being hospitable in giving me an office during this period equipped with high quality equipment (as well as an office mate). For surrounding me with a great work environment and wonderful employees.

I would also like to thank my examiner Henrik Ström for his support and for helping with everything surrounding the thesis.

This thesis was partially supported by the Production Area of Advance at Chalmers and the computations performed were enabled by resources provided by the Swedish National Infrastructure for Computing (SNIC) at Chalmers Centre for Computational Science and Engineering (C3SE)

David Andersson
Gothenburg
June 2023

Contents

1

Introduction

Today, in a society with ever more focus on environmental requirements and footprints, the automotive industry, among many others, face large transformations of the older manufacturing methods. Together with the emerging and rapidly increasing power and accuracy of virtual manufacturing tools the possibilities arises for optimized output with regards to both economical and environmental aspects readily available for anyone. One crucial set of sub processes in the manufacturing stage which has significant potential for the emerging virtual tools are the surface treatment processes. The surface treatment in modern automotive industries can stand for up to 40% of the energy consumption during manufacturing and is the single most demanding process with regards to water, energy and chemicals [1]. While it is one of the processes which generates the most pollution and waste products, it is simultaneously one of the most important processes for durability and protection from wear as well as appearance of the car. The bodywork is protected by several layers of different coatings including pre-treatment which removes pollutants, electrocoating which protects from corrosive decay followed by at least three layers of paint in the form of primer, base and clear coat layers. The surface treatment also consists of the application of sealing materials with the objective to fill cavities which otherwise would be sources of noise and moisture. The CO_2 emissions for a whole car treated in modern paint shops are therefore on the order of 140 kg/car [1], or more for older paint shops, which is equivalent of driving a gasoline car in Sweden for approximately $892\,km^*$ [2].

Optimizing, or generally reducing the environmental impacts of the surface treatment is therefore an important step in creating a sustainable automotive manufacturing industry. Especially as the industry has started to significantly shift towards electric vehicles and the footprint of the production becomes the dominating life time contributor to the emissions of the car.

*The estimate is assuming an average pollution production from combustion of 31.4 tons of CO_2-equivalent per lifetime and with an average lifetime of 200 000 km

1.1 Background

This thesis will focus on the painting aspects of the surface treatment process and the following subsection will cover a brief introduction to the process and its theory together with some of the main challenges involved when attempting to model it.

The painting process in modern automotive paint shops are performed by large industrial robots most commonly equipped with an *Electrostatic Rotary Bell Sprayer* (ERBS) applicator. The rotating bell applicators are normally preferred over air sprays due to larger *Transfer Efficiencies* (TE) [3], which is the ratio between the amount of paint hitting the target and the total amount of paint ejected from the applicator. The fundamental functional procedure of any rotating applicator is that paint is released from the bottom of the bell and forms a thin film which is driven towards the edges due to centrifugal forces caused by the high angular velocity. At the edges, the paint film is atomized into fine particles which are directed down towards the target by a strong shaping airflow which envelopes the bell from above. A geometric view of this description can be obtained in Figure 1.3a.

The ERBS technique also provides the paint particles with an additional electrostatic force not available in air sprays. By electrically charging the particles at the applicator they will produce a force field directed towards the grounded target. This also has the effect of spreading out the particles more evenly in space due to charge repulsion. Yasumura et al. [4] reported that the effectiveness of the two different directing techniques - shaping airflow and electrostatic force field, was dependent on the particle size, where smaller ($<10\mu m$) and larger ($>60\mu m$) particles were mostly affected by the shaping airflow, and the particles with sizes in between were more effected by the electrostatic forces. The mean particle size for a rotating atomization process such as the ERBS is dependent, assuming a given applicator and a given specific paint, only on the paint flow rate and the angular velocity of the bell [5]. Smaller particles generally results in smoother finishes but with lower TE and larger particles generally in the reverse [3]. Therefore the ideal spray has particles of uniform size which would result in the most predictable finishing result as possible. To achieve varying optimized finishing results, such as e.g. maximized TE or optimal paint thickness there are a large array of settings which can be selected in the different parts of the described paint process. Many of the settings in the optimization process are related to the applicator and how the paint particles are injected into the domain. These settings are important and offer many degrees of freedom to the optimization which makes it both flexible and resource demanding.

Due to the strong shaping airflow the near-bell region is most commonly treated as compressible [6, 7] which is a flow property that requires a fine spatial resolution as well as a detailed temporal integration in order to be resolved by a *Computational Fluid Dynamics* (CFD) simulation. In large industrial applications however it is not feasible to run large scale compressible simulations due to the large differences in scales, both temporal and spatial,

within a full paint job of an object [1]. The scales of the high velocity flow near the paint injection are fundamentally different from the scales of painting an entire part which often is on the order of dozens of seconds.

Fraunhofer Chalmers Center (FCC) has developed a flow solver which is specifically aimed at the issue of incompatible scales [1, 8]. The flow solver, called IBOFlow (Immersed Boundary Octree Flow Solver) is a continuum based solver adding both multiphase and multiphysics features. As the name of the model infers, it uses an octree based approach for spatial discretization and storage, greatly facilitating dynamic refinement and coarsening of the structured grid. This feature enables the solver to handle moving objects well because the grid can be refined around its boundary without any significant computational cost. The solution for the issue of scales is a decomposition where the resource demanding smaller scales near the rotating bell are solved separately and subsequently imported as a static boundary condition to a coarser simulation which extends the spatial and temporal scales. IBOFlow does currently not possess a compressible solver which means that the smaller scales are simulated using either commercial or open source software.

1.2 Virtual Paint Shop

IBOFlow is a central part of the large scale ambition to sustain a virtual paint shop to be used in industrial automotive applications. A virtual paint shop is meant to act as a virtual clone of the actual environment and equipment in the industrial paint shop and to thereby accurately be able to simulate it. Thusly both the procedural and the detailed oriented work can be subjected to optimizations without the necessity of spending physical resources.

The virtual paint shop consists of viscoelastic sealing of the vehicle body [9], externally or internally charged ERBS spray painting applications [10] where the paint can either be a liquid or a powder. It also consists of the corresponding oven curing stage required for each layer of paint applied [11, 12] as well as the optimized robot paths which become required when painting over complex geometries [13].

Heretofore the virtual tools for the surface treatment in the automotive industry have not been incorporated into the manufacturing process to the same degree as many other have [1]. The robot paths and process parameters are manually fine tuned in a slow and resource demanding trial-and-error process which involves painting prototypes and subsequently washing them off to be painted again. With the emergence of the accurate and robust virtual paint shops the product conceptualization process can be revamped to include paint trials already in the design phase and to eliminate most, if not all, need for prototype testing.

All of the mentioned complex steps involved in the surface treatment process are included in the IPS Virtual Paint software distributed by *Industrial Path Solutions* (IPS) IBOFlow AB. The ERBS spray paint simulation used in the IPS software uses IBOFlow and it is therefore

at this macro level that this thesis is situated.

1.3 CFD Software

The following section introduces the reader to the underlying details of the physics behind the spray paint modeling implemented in the CFD software used in this thesis. The section will firstly cover the prominent governing equations used in the multiphase and multiphysics solver and subsequently introduce some of the unique features of the simulation techniques.

1.3.1 Governing Equations

The governing equations will be presented for the three main physical phenomena captured by the solver; fluid dynamics, electrostatic physics and dispersed particulate physics.

1.3.1.1 Fluid Field

The fluid is modeled using the incompressible formulation of the Navier-Stokes equations and time averaged, resulting in the *Reynolds Average Navier Stokes-* (RANS) equations in Equations (1.1) and (1.2). The momentum equation is seen in (1.1) and the continuity equation in (1.2).

$$\frac{\partial \overline{u}_i}{\partial t} + \overline{u}_j \frac{\partial \overline{u}_i}{\partial x_j} = -\frac{1}{\rho}\frac{\partial \overline{p}}{\partial x_i} + \frac{\partial}{\partial x_j}\left(\nu\left(\frac{\partial \overline{u}_i}{\partial x_j} + \frac{\partial \overline{u}_j}{\partial x_i}\right) - \overline{u_i' u_j'}\right) + \overline{s}_i \tag{1.1}$$

$$\frac{\partial \overline{u}_i}{\partial x_i} = 0 \tag{1.2}$$

Where $\overline{u}_i$ is the mean field velocity of the fluid in the i^{th} dimension, $\overline{p}$ is the mean field pressure, ν is the fluid kinematic molecular viscosity, $-\overline{u_i' u_j'}$ are the so called Reynolds stresses and $\overline{s}_i$ are additional source terms e.g. gravity and momentum transfer from the dispersed phase.

To close the currently unclosed RANS formulation the Reynolds stresses are modelled as a turbulent viscosity according to the Boussinesq assumption, resulting in

$$\frac{\partial \overline{u}_i}{\partial t} + \overline{u}_j \frac{\partial \overline{u}_i}{\partial x_j} = -\frac{1}{\rho}\frac{\partial \overline{p}}{\partial x_i} + \frac{\partial}{\partial x_j}\left((\nu + \nu_t)\left(\frac{\partial \overline{u}_i}{\partial x_j} + \frac{\partial \overline{u}_j}{\partial x_i}\right) - \frac{2}{3}\delta_{ij}k\right) + \overline{s}_i \tag{1.3}$$

Where ν_t is the turbulent viscosity and the additional term $\frac{2}{3}\delta_{ij}k$ is to ensure a non-zero trace of $-2k$

IBOFlow uses the $k-\omega$ SST turbulence model, i.e. it uses the $k-\omega$ in the boundary layers around objects and a $k-\varepsilon$ like behavior farther from the boundaries. The expression for the turbulent viscosity is then defined as:

$$\nu_t = \frac{a_1 k}{\max(a_1\omega\,,\, F_2 S)} \tag{1.4}$$

Where k is the turbulent kinetic energy, ω is the specific turbulent dissipation rate, F_2 is a blending function, S is the magnitude of the strain rate $\sqrt{2S_{ij}S_{ij}}$ where $S_{ij} = \frac{1}{2}\left(\frac{\partial u_i}{\partial x_j} + \frac{\partial u_j}{\partial x_i}\right)$ and a_1 is a standard parameter associated with the $k-\omega$ SST model. k and ω are solved by a respective transport equation not included in this thesis.

The governing fluid equations are solved using the finite volume method which is discretized using a dynamic octree structured grid with collocated cells. The equations are solved segregated hence requiring a pressure-velocity coupling scheme selected to be the SIMPLEC method which is combined with Rhie and Chow interpolations to avoid pressure oscillations [1].

1.3.1.2 Electrostatic Field

The electrostatic field in the domain is determined by

$$E_i = \frac{\partial \phi}{\partial x_i} \tag{1.5}$$

Where ϕ is the electric potential between the particle and the grounded target obtained from the following Poisson equation:

$$\frac{\partial^2 \phi}{\partial x_i x_i} = -\frac{\rho}{\varepsilon} \tag{1.6}$$

Where ρ is the particle space charge density and ε is the electric permittivity of air.

Equation (1.6) is solved using the finite volume method and discretized on a dynamic octree grid which in general is different from the fluid discretization grid.

This thesis will, in order to keep some of the complexity down, disable the use of the electrostatic solver in IBOFlow. This will ensure that the effects of the fluid-particle coupling is maximized even though this is not a realistic condition. An inclusion of the electrostatic forces will in general reduce over sprays since the paint will be driven towards the grounded target by additional forces.

1.3.1.3 Dispersed Phase

The dispersed paint particles are modeled using a force balance including the effects of gravity, buoyancy, drag and electrostatic forces [1], seen in Equation (1.7)

$$\rho_p \frac{d\overline{u}_p}{dt} = (\rho_p - \rho_f)\overline{g} - \frac{\rho_p}{\rho_f}\frac{m_p}{2r_p} C_d \, \overline{u}_r \, |\overline{u}_r| + \overline{E} q_p \tag{1.7}$$

Where ρ_p and ρ_f are the particle and fluid density respectively, m_p is particle mass, r_p is the particle radius, C_d is the drag coefficient, $\overline{u}_r$ is the relative velocity between the particle and the fluid, $\overline{E}$ is the electric field and q_p is the particle charge.

The time integration is performed with a forward Euler scheme, where each particle has its own local time step which in general is smaller than the shared time step of the fluid and electrostatic fields.

The drag coefficient C_d is obtained as

$$C_d = 24 \, \frac{1 + 0.15 Re_p^{0.687}}{Re_p} \tag{1.8}$$

Where Re_p is the particle Reynolds number defined as

$$Re_p = \frac{2 r_p \, \rho_f \, |\overline{u}_r|}{\mu} \tag{1.9}$$

Where μ is the fluid dynamic viscosity.

The fluid and the electric fields are interpolated to the position of the particles where Equation (1.7) is evaluated. The resulting drag force and electrical charge from Equation (1.7) are subsequently interpolated back to the respective grid of the two fields. The drag force is included in the source term $\overline{s}_i$ in Equation (1.3) and the charge is used to obtain ρ in Equation (1.6). Thus establishing the particle-fluid and particle-electric two way coupling. The particle-particle coupling is neglected as the multiphase flow is assumed dilute further away from the bell [1]. For externally charged ERBS applicators there is an additional coupling between the fluid and the electrostatic field, for internally charged ERBS applicators there is only the weak coupling through the particles. This is further described in detail in [14].

Since a normal spray paint applicator releases paint particles on the order of 10^9 particles per second [15] the particles are conglomerated into computational parcels or point clouds for improved efficiency. The parcels in IBOFlow are voidless, averaged and created such that all parcels either have the same surface area or volume, meaning that parcels representing smaller particles will consist of many more particles than a parcel representing large ones. Constant surface area of the parcels provides a more stable drag force as it can control for

small values of r_p in Equation (1.7). The terms *particles* and *parcels* will be used somewhat interchangeably throughout this thesis to facilitate intuition rather than strict correctness, but every time particles are mentioned in association with modeling aspects in CFD it is really meant as parcels.

The local velocity fluctuations in the fluid flow, which have been filtered out by the RANS time averaging filter, are re-introduced artificially for the particles using a *Discrete Random Walk* - (DRW) model [8]. The direction is sampled from a random point on a unit sphere and magnitude noise is determined through the kinetic energy at that location.

1.3.2 Methods of Simulation

In the following subsection methods regarding some of the characteristic simulation techniques used in IBOFlow are presented. The methods include the way IBOFlow handles physical objects, such as the paint target or the applicator, in the domain. It also describes in more detail the computational domain decomposition for the temporal and spatial scales, as well as a brief and general description of how the final paint thickness is computed.

1.3.2.1 Immersed Boundary Method

IBOFlow uses a special *Immersed boundary* (IB) technique to track the presence of objects such as the applicator itself or the paint target in the fluid [1]. The IB-method is a Lagrangian boundary tracking technique used inside the Eulerian fluid discretization, hence there is no re-meshing required of the fluid grid as the object traverses the domain.

Typically the IB-method can suffer from accuracy problems. Mark et al [16] suggests this is related to unphysical mass fluxes and boundary conditions over the IB and proposes a novel approach in [16, 17]. The method creates fictitious velocities inside the IB which enforces that the fluid velocity at the boundary is equal to the velocity of the moving object - in line with the no slip boundary condition.

In order for the fluid grid to be aware of the moving IB, the cells close to boundary of the object are marked. The marked cells are denoted as *mirroring cells* and are formally classified as such if the cell center lies inside the IB and the minimum distance to the IB is smaller than one and a half cell size. One cell is associated with one point on the IB and more IB points is in general associated with higher accuracy of the model [17]. Thus, in some instances of e.g. large curvatures, the distance from a mirrored cell center to the IB could be increased to ensure a well defined resolution of the IB. A simple schematic image of a two dimensional view of the immersed boundary capturing of a circle is seen in Figure 1.1.

The mirrored cells are obtained from an padded octree block search around the IB, capturing the cell centers along with its associated distance d from the IB. To ensure that the fluid accounts for the presence of the IB, the *immersed boundary condition* (IBC) of each IB point

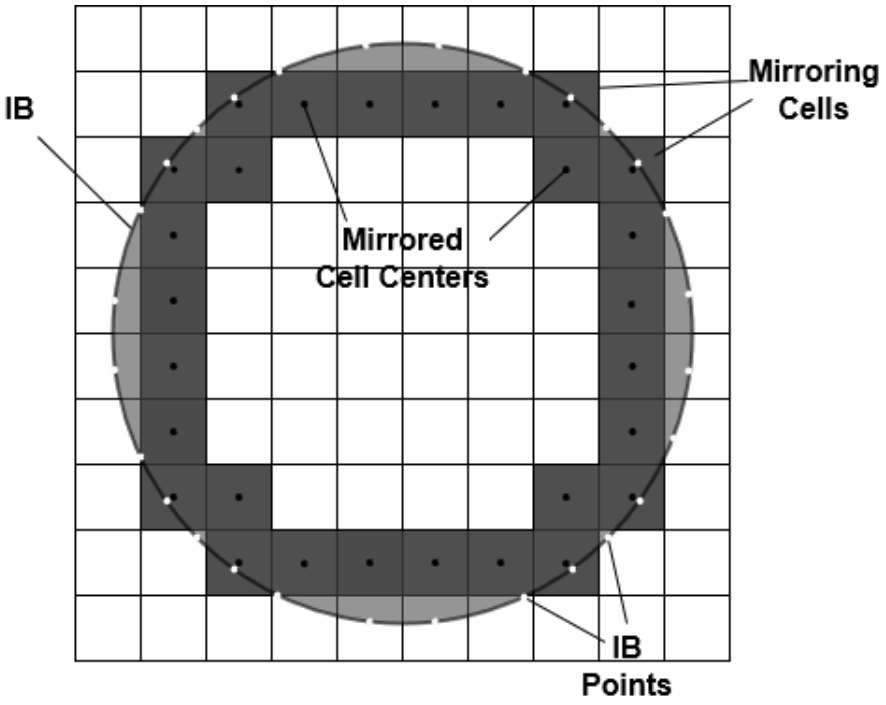

Figure 1.1: A visual demonstration of the cell classifications based on the presence of a circular immersed boundary. Each mirrored cell center (black dot) is associated with one point on the immersed boundary (white dot)

needs to be communicated and enforced on the fluid discretization. The goal is to be able to interpolate the known velocity of the IB to the mirrored cell centers, but in order to do this an additional point where the velocity is known needs to be extracted as the second reference.

The third point, denoted $\mathbf{P}_e$, is obtained from a symmetric mirroring condition where the mirrored cell center $\mathbf{P}_m$ and $\mathbf{P}_e$ are at equal distances from the IB, see Figure 1.2. The expression for $\mathbf{P}_e$ is found in Equation (1.10).

$$\mathbf{P}_e = \mathbf{P}_m + 2d\,\hat{\mathbf{n}} \tag{1.10}$$

Where d is the distance between the mirrored cell center and the IB, and $\hat{\mathbf{n}}$ is the unit vector pointing from the cell center to the closest point on the IB.

As the third point is established inside the fluid field, its velocity can be obtained by trilinear interpolations. The known velocity of the IB, $\mathbf{u}_{IB}$, can susequently be communicated to the mirroring cell center through a simple rearranged average formula in Equation (1.11).

$$\mathbf{u}_m = 2\mathbf{u}_{IB} - \mathbf{u}_e \tag{1.11}$$

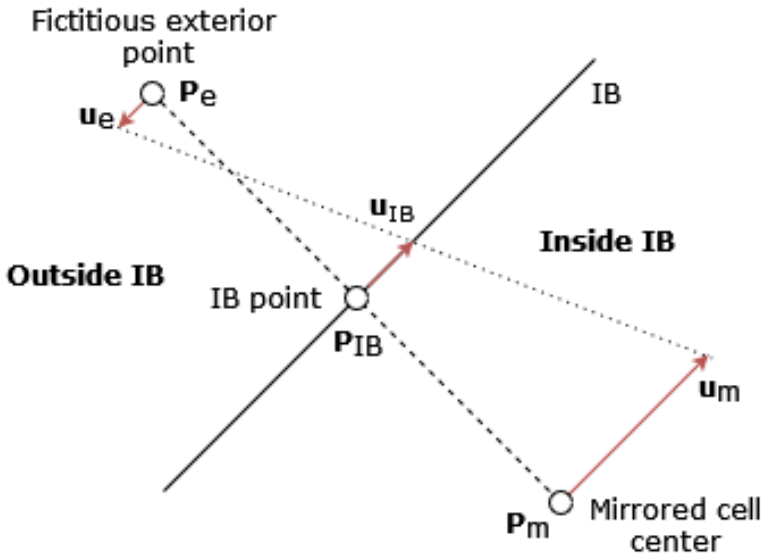

Figure 1.2: The mirroring process in a mirroring cell done in order to obtain the second reference point $\mathbf{P}_e$

The effect of this is that the velocities of the mirroring cells can now be used as additional references when performing interpolations over the neighboring cells. Important to note is that the velocities $\mathbf{u}_m$ are entirely fictitious and located inside the immersed object. It would, if used in the continuity equation induce unphysical mass fluxes across the IB. Therefore, to ensure mass conservation, it is excluded in that discretization. Due to this a pressure field will appear around the IB as an artifact from the pressure velocity coupling so that fluid entering a cell must leave it from any face which is not normal and adjacent to the IB.

1.3.2.2 Domain Decomposition

Currently IBOFlow utilizes a decomposition due to the issue of scales described previously where the domain is partitioned into two separate parts. The first part solves the smaller scales in the near-bell region (the combined regions of 1 and 2 in Figure 1.3b) with a detailed compressible simulation performed using an external CFD software. The larger scales (region 3 in Figure 1.3b) are solved with an incompressible and coarser simulation using IBOFlow which solves for the spatial domain with physical time. The near-bell region is currently time averaged and used as a static boundary condition in the coarser simulation. The near-bell region is therefore only a "read-in" zone in IBOFlow, solving no physics and can thus extend the scales efficiently. The boundary condition is communicated to the fluid field through trilinear interpolations.

1.3.2.3 Particle Injection

Depending on if particles are injected or if a pure airflow is simulated the imported fluid boundary condition is different. There are different external simulations which have been

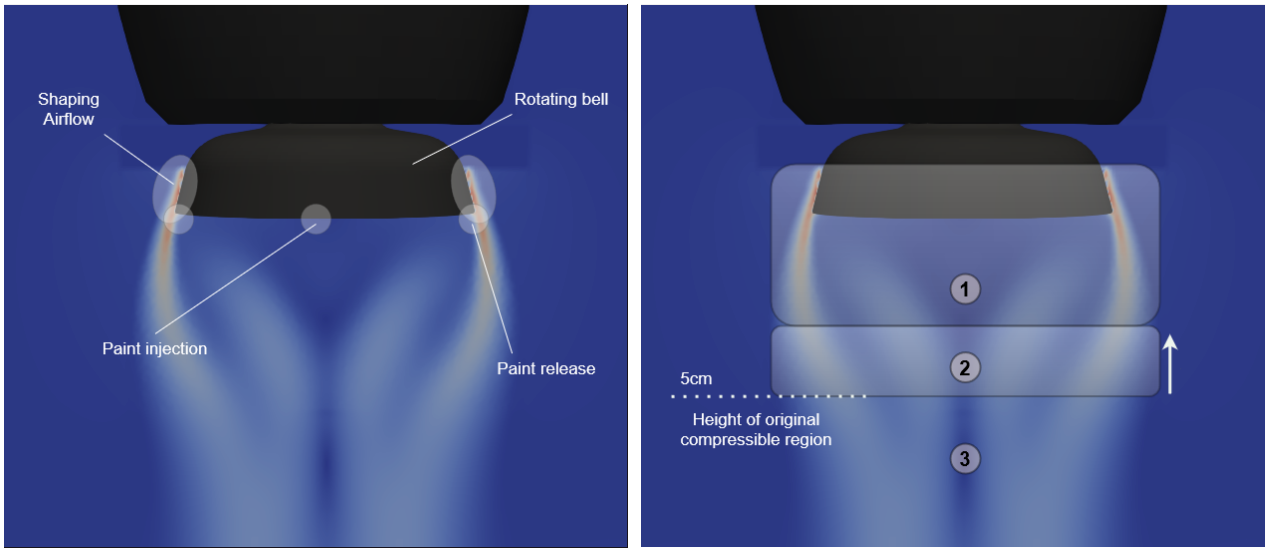

(a) The rotating bell geometry

(b) Different regions of the computational domain

Figure 1.3: Details about the rotating bell used in the simulations

run with particles and without. Additionally, there are different external simulations which correspond to varying bell settings of the particle injection. Different injection parameters result in different airflows which impacts the flow development in IBOFlow.

In real, physical, applications the settings which are used to control the paint injection and, as consequence, the finishing result are for example the strength of the shaping airflow, the paint flow rate or the electric charges, as alluded to in Section 1.1. The different physical settings result in different break-up behaviors which are difficult to predict and in general undesirable to simulate. Therefore IBOFlow utilizes *injection parameters* instead which has the effect of parameterizing the complex break-up behavior. The injection parameters are related to physical phenomena which occur during the break-up such as the particle size distribution or momentum loss. Parametrizing the break-up behavior removes much complexity, but simultaneously introduces the requirement to perform parameter optimization studies to know which values each parameter should take. The target for the optimization studies are experimentally obtained finishing results which are obtained using the real, physical, bell-settings according to the demands of the costumer. The parameter optimization is therefore the process of attempting to match several injection parameters in such as way so that it minimizes the difference against that experimental data.

1.3.2.4 Domain Specification

The computational domain used in this thesis is constructed such that the bell is always located in the middle of an enveloping block representing the surrounding domain with size $(1.1, 1.1, 0.4)\,m$ in the x, y and z-direction respectively. The coordinate system is placed

such so that the height (z-coordinate) of the origin is placed at the height of the paint injection, pointing downwards. The other components of the origin is placed directly in the middle of the domain.

The placement of the compressible boundary condition zone is between $-2\,cm$ and $5\,cm$ in the z-direction and symmetrically in the x-y-directions between $-4.75\,cm$ and $4.75\,cm$.

On the top of the domain a velocity inlet boundary condition is placed with a small down draft similar to that in a paint booth. The other five faces employ a pressure outlet condition, commonly used for faces opposing inlet conditions. The boundary values for the pressure is determined by checking the direction of the flow; where if it is an inflow the total pressure is specified and if it is outflow the pressure is set to the ambient pressure.

1.3.2.5 Paint Thickness

Validating the results of a paint simulation against a real part requires that the paint thickness is computed. As mentioned in Section 1.3.1.3 *Dispersed Phase* the particulate part of the simulation is simplified by the use of computational parcels. Therefore the paint thickness estimation must in some way account for the smaller than realistic sample size.

IBOFlow implements a grid independent thickness model based on kernel density estimation [15] which is commonly used to construct *probability density functions* (PDF) given a limited amount of sample points. The paint thickness curve is thus approximated as a PDF by super positioning the distribution around each sample point created by a kernel function K [18], see Figure 1.4. The kernel function is most commonly selected to be a Gaussian distribution function, but could be any function formally constrained by:

- $\int_{-\infty}^{\infty} K(x)\,dx = 1$
- $K(-x) = K(x)$
- $K(x) \geq 0 \;\; \forall x \in \Re$

An essential associated component of K is the smoothing bandwidth denoted h. The bandwidth controls the width of the kernel function, where smaller values of h draws the kernel towards a delta-function and therefore does not adapt well to smaller sample sizes. Larger values of h on the other hand draws the kernel function towards a flattened line, smoothing out important details. It is therefore clear that values of h are of great importance for a well defined and sufficiently detailed PDF, but also that it simultaneously is semi-arbitrarily chosen based on the data set.

The somewhat intricate details of the kernel density method in [15] are omitted, but Tafuri et al reports good improvements in the numerical accuracy of the paint thickness estimation compared to more common methods such as binning.

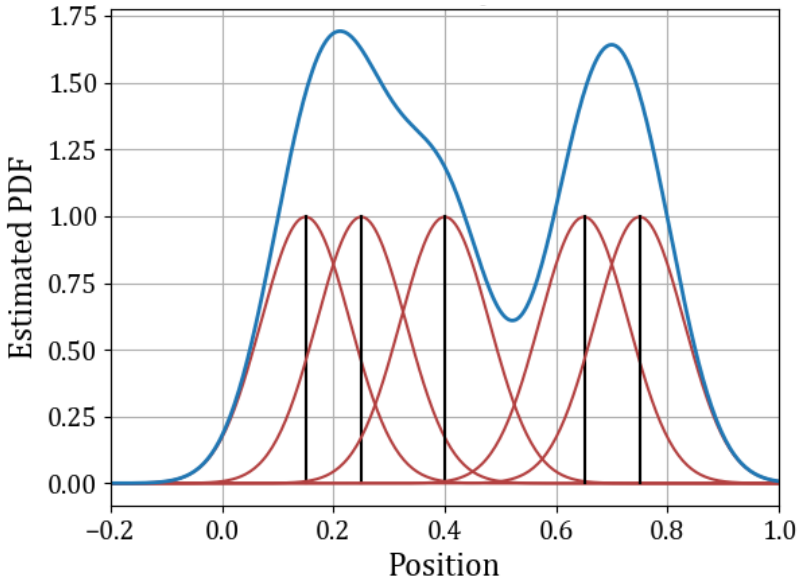

Figure 1.4: A probability density approximation in 1D (blue curve) based on the super position of all kernel distributions (red curves) which are defined around the sample points (black lines). The bandwidth h used was 0.4.

1.4 Motivation

The two part decomposition used by IBOFlow, described in Section 1.3.2.2 *Domain Decomposition*, currently requires a new compressible simulation every time any of the bell settings are changed. As the bell settings are often updated many times in the optimization procedure the overhead of this process becomes especially resource demanding due to the large set of degrees of freedom. Each optimization is also somewhat unique to the specific finishing demands or the geometry of that case. Altogether this leads to both limited reusabillity and large optimization spaces which further obstructs good resource management.

It would therefore be desirable in terms of computational efficiency to establish a separate region 2, see Figure 1.3b, which is simulated incompressibly in IBOFlow. The size of region 2 is desired to be maximized and to cover the whole paint injection area, not including the $2\,cm$ above the bell. This area will still be imported as a compressible boundary condition but, since no particles are injected there, it can ideally be simulated only once and used for every single injection case. Region 2 will, similarly as for the two-part decomposition, also be treated as a static boundary condition in the coarser simulations, obtained by time averaging the fluid field over a certain time span.

Other work has been done for comparing the validity of an incompressible simplification compared to solving the compressible equations in more general cases such as turbulent water droplets [19, 20]. Bukhvostova et al. [19] simulated water droplets including mass and heat transfer between the phases at different Mach numbers (Ma). It was found that the inertial properties of the fluid, such as velocity and Reynolds number were matching

closely, with a maximum error of 2% for $Ma = 0.2$. Similar conclusions were found in [20] where there was approximately a 1% difference between a compressible and an incompressible formulation to the governing equations.

1.5 Aim

The aim of this master thesis is to investigate the validity of a simplification of the simulation process in IBOFlow where only one, smaller, compressible simulation is required from an external CFD software, and the remainder of the domain is solved incompressibly by IBOFlow.

1.6 Limitations

The work in this thesis was limited by the bottle neck constituted by the relatively large simulation times required for many of the simulations. Typical simulations with sufficient details took between 30 and 48 hours on the Chalmers Clusters using an NVIDIA A40 graphics card and where a personally allocated time provided restrictions for the total amount of usage.

1.7 Delimitations

The scope of this thesis was delimited by placing most of the validating efforts based on the errors of the resulting flow field, not the estimated paint thickness distributions. Section 3.2.2 does present thickness estimations to the corresponding airflow cases studied there, however this evaluation was mostly an ad-hoc addition to the thesis. It is left as future work to go into more details regarding the resulting paint thickness distributions as a function of varying injection parameters or compressible heights.

1.8 Problem Statements

The following problem statements are guiding the central narrative of the thesis and are aimed to be answered during the process.

- Can a pure airflow simulation near the bell be partitioned to some degree into compressible and incompressible parts while keeping sufficient accuracy?
- Can an air-particle simulation using the near-bell incompressible partition be sufficiently equivalent to the fully compressible case?
- Can the same compressible airflow be used for different particle injection parameters while keeping sufficient accuracy?

1.9 Ethical and Ecological Aspects

The surface treatment is, as previously mentioned, the part in the automotive manufacturing process which requires the most energy, water and chemicals. It is additionally associated with large generations of waste and air pollutants which therefore necessitates good systems for ventilation. Insufficient levels of ventilation could cause a large spread of hazardous air-pollutants in the working environment making it difficult or impossible for humans to be involved without serious precautionary measures.

The current work at FCC for developing the virtual paint tools enables the painting process to become both more efficient and also decreases the need of, otherwise required, prototype tests. A removal of prototype testing or an increase in computational efficiency could result in large energy savings and reductions in waste and pollutants.

The role of this thesis is to aid the development of this virtual paint environment by improving the efficiency of the simulation process. Better efficiency when performing the simulations lead to a much faster turnover rate of different bell settings which with a combination of well tested and reliable results could help to increase the rate of which the virtual surface treatment processes are included in the modern industry today.

2

Methods

The methodology in this thesis was divided into two separate parts where the first part was a study without using paint but simply studying the time evolution of the airflow and how it behaved to an incompressible simplification. The second part was a coupled fluid-particle simulation which was based on the result of the pure airflow simulation. Simulating the pure airflow reported, using the most simple conditions available, the smallest compressible height for which the incompressible simplification could still run accurately. That height would subsequently be the limit in all remaining studies.

A cross validation was also performed for the fluid-particle simulations. Since one of the aims of the thesis was to investigate how well a single compressible boundary condition would work on a simulation where the injection parameters were different, this study systematically investigated the impact of three different injection parameters. The injection parameters studied were *slip factor*, *axial velocity* and *particle size*, or so called *dv50*, which are all described in further detail in Section 2.3.3 along with the methodology used. With the current decomposition the main injection parameters used for paint optimizations are the dv50 and the particle charge. This thesis excludes the electrostatic solver, as mentioned in Chapter 1 and therefore includes the two other injection parameters; slip factor and axial velocity instead. Of the three, the dv50 injection parameter is therefore the most important with respect to the current state of operations.

2.1 General Validation

The fundamental approach to all validations used in this thesis was to define a validation volume located in some distinct region where the error-measurement was to take place. The validation volume was cylindrical and contained a separate grid of validation points in all three dimensions placed independently on the fluid discretization. The validation metric, further described in Section 2.1.1, was evaluated at the validation points, to which the fluid field was communicated using a trilinear interpolation scheme.

2.1.1 Validation Metric

The validation metric used to validate two simulations based on the fluid data was the magnitude of the fluid velocity difference between the simulations. To avoid a naïve error estimation, where the error was a simple average of velocity differences of the validation points, a weighted error was implemented. The simple averaging method was considered naïve because the validation grid points were not selected to be representative of the flow characteristics in the validation volume. This meant that the error had a risk of being dampened by points placed in non-critical regions where the velocity magnitude of the flow was low and thereby also the velocity difference between the two simulations.

Instead the weighted average was utilized, where the weights were selected to signalize the relative importance of the sampled point. The advantage of a well defined weighted average is that the error becomes more or less independent on the number of validation points it is evaluated at.

The equation for the weighted error is seen in Equation (2.1), and the weight is defined in Equation (2.2)

$$error = \frac{\sum_{points} w \cdot \|\mathbf{v} - \mathbf{v}'\|}{\sum_{points} w} \tag{2.1}$$

Where $\mathbf{v}$ is the velocity vector for the current simulation, $\mathbf{v}'$ is a reference velocity and w are the weights defined in Equation (2.2).

$$w = \frac{\|\mathbf{v} - \mathbf{v}'\|}{\|\mathbf{v}\|} \tag{2.2}$$

The size of weights are proportional to the velocity error, normalized on the physical velocity at that point, resulting in a dimensionless and bounded weight.

2.1.2 Normalization

The error in Equation (2.1) is currently defined in absolute terms of velocity magnitude. In order to be able to relate the error to the given flow it is desirable to normalize the error by a characteristic velocity and thereby obtaining a dimensionless error. The characteristic velocity was chosen to be the maximum velocity captured in the whole domain which was $120\,m/s$. The error, or the weighted velocity difference between two simulations, thereby reads as a percentage of the maximum velocity.

2.2 Methodology Without Using Particles

Previous sections were a common description on the methods of validation used throughout this thesis regardless whether particles were used or not. The following section specifies the methodology for the case where a pure airflow was simulated.

2.2.1 Mesh Convergence

To ensure a numerically and physically stable mesh convergence two complimentary studies were made aimed to eliminate these sources of errors. Firstly a temporal convergence was carried out in order to determine at what time the solution had sufficiently converged. Secondly there was a convergence of the fluid time step with the objective to obtain a stable *Courant-Friedrichs-Lewy* - (CFL) number to be used during the mesh convergence.

The CFL number in IBOFlow is implemented as an outflow CFL, which for a given cell is defined as:

$$CFL = \frac{u_i \Delta t}{\Delta x_i} \tag{2.3}$$

Where u_i is the fluid face velocity for face i where the fluid is leaving the cell, Δt is the local time step and Δx_i is the size of face i.

Equation (2.3) uses Einstein's convention for summation, hence the maximum CFL for a typical three dimensional case can also be written as:

$$CFL = \Delta t \left(\sum_{i=1}^{3} \frac{u_i}{\Delta x_i} \right) \leq CFL_{max} \tag{2.4}$$

While performing the grid convergence the CFL number obtained from the time step convergence was ensured to remain constant as in [21, 22], removing additional potential numerical sources of errors. This was simply done by adjusting the fluid time step by the same factor as the mesh size was refined. The domain size was kept constant at $(1.1,\ 1.1,\ 0.4)\,m$ for the x, y and z-direction respectively and the mesh size was controlled implicitly by changing the number of grid points in each direction for the coarsest refinement level.

The mesh convergence was performed with a fully compressible near-bell boundary condition ending at $5\,cm$ below the bell.

2.2.1.1 Validation

Since the compressible height remained constant over all simulations during the mesh convergence the validation volume was placed below the compressible boundary condition. The size of the volume was made relatively small, $1\,cm$, so that it would in principal only capture

the error originating from the transition between the compressible part and IBOFlow, not accumulate over a larger region. The grid density was defined with 25 points in the radial direction and 10 points in the z-direction. The validation region can be seen in Figure 2.4, marked *static validation volume*.

2.2.1.2 Convergence of Complimentary Studies

The result of the complimentary studies which were carried out prior to the mesh convergence were validated in accordance of Section 2.1 *General Validation* as well as Section 2.2.1.1.

The study for Δt convergence was executed first, simulating for 0.1 seconds on a standard mesh size for a variable Δt. The finest value of Δt, $0.01\,ms$, was used as the reference in the error defined in Equation (2.1), and the error was subsequently normalized on $120\,m/s$ which was the largest velocity in the domain. The resulting convergence propagation can be seen in Figure 2.1a where an applied convergence tolerance of 1e-3 results in a converged Δt of $0.07\,ms$. In a similar procedure the time convergence was run for 0.1 seconds on the same mesh but now using the converged time step. Using the same convergence tolerance, the physical time converged at 0.02 seconds, as seen in Figure 2.1b, thus placing the converged Δt well within the converged margins with regards to time. Hence the temporal parameters were selected to be $0.02\,s$ for physical time and $0.07\,ms$ for the fluid time step resulting in a stable CFL number at 6 which would remain constant over any mesh refinements.

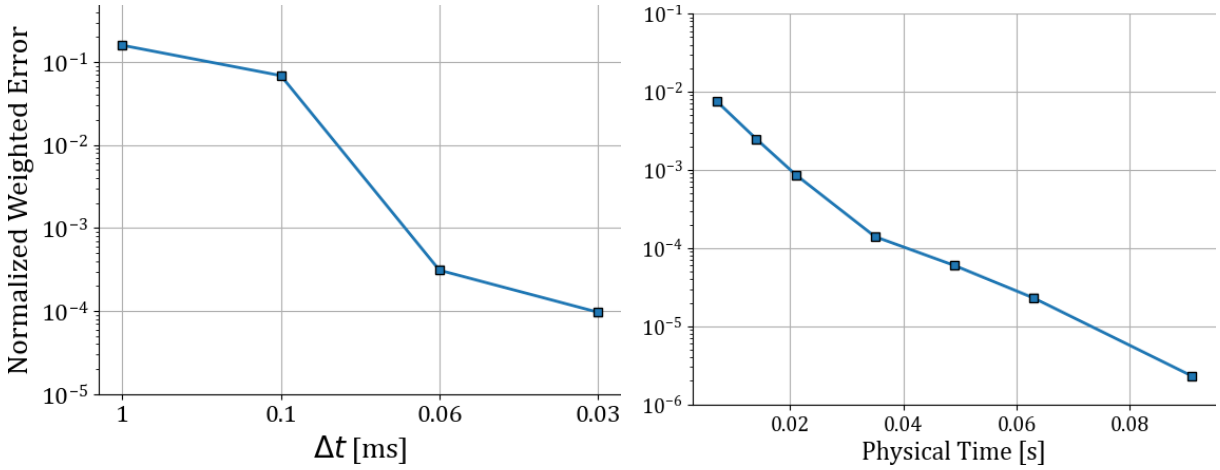

(a) Convergence of the fluid time step **(b)** Convergence of the physical time

Figure 2.1: Convergence of the complimentary studies prior to the mesh convergence

2.2.1.3 Convergence of Mesh Size

Once the complimentary studies were completed the mesh convergence study could be performed without numerical or physical discrepancies. The study was carried out using five different meshes at constant CFL, each one refined by a scaling factor from the base mesh size, see Table 2.1. The mesh structure remained the same over the study and was refined

with increasing detail closer to the bell using several *refinement levels*, see Figure 2.2. Each refinement level halved the cell size in all directions. In the most refined zone the refinement level was set to 4. The grid in the compressible zone was not refined as much as where the validation volume was placed since the refinement of these cells would not impact the physics of the simulation for a pure airflow.

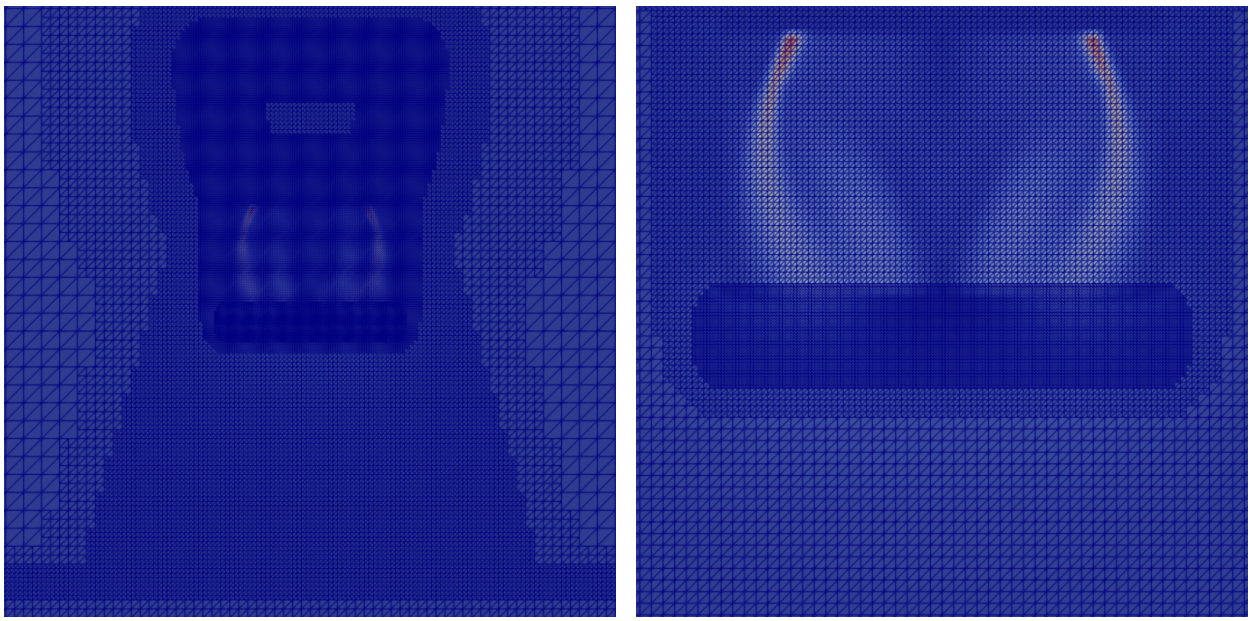

(a) Refinement increase close to the bell **(b)** Mesh refinement in the validation region

Figure 2.2: Illustration of the mesh refinement structure used in the mesh convergence study

Table 2.1: Details of the mesh convergence study

Case	**Refinement Factor**	**Smallest Cell** [mm]	**Cell Count** (millions)	Δt [s]
1	0.75	0.833	2.0	9.33e-5
2	1	0.625	4.6	7e-5
3	1.25	0.500	9.9	5.6e-5
4	1.5	0.416	16.8	4.66e-5
5	1.75	0.357	26.7	4e-5

The mesh convergence resulted in Figure 2.3 where the finest mesh size, case 5, was used as the reference. It can be seen that the errors plateaus for finer mesh sizes close to the previously used convergence margin. Since the difference in the error is so marginal and since the computational effort required for the finer meshes increases two-fold, both by

lowering the time step as well as increased iteration time, the base mesh size according to Case 2 was deemed to be appropriately converged for the purposes of this thesis.

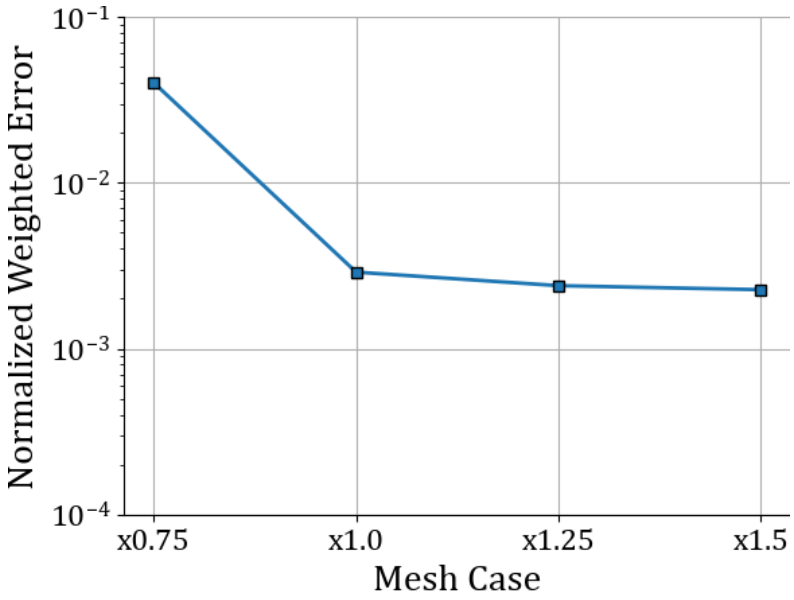

Figure 2.3: Result for the mesh convergence study where the errors where computed using the finest mesh of x1.75 number of grid points compared to the base mesh

2.2.2 Compressible Height Convergence

As described in Chapter 1, the investigation of to which height the compressible region could be lifted up to, was one the main aims of the thesis. The investigation involved increasing the sizes of the incompressible region (see region 2 in Figure 1.3b), in discrete steps and for each step simulate the case in IBOFlow. Thus establishing the region of an incompressible simplification. Naturally the amount of the domain which was boundary conditions continually decreased, thus exposing more and more of the previous compressibly obtained values to the incompressible simplification. The term for this area will in the continuation be referred to as the *compressible delta region*. Since the values that continually got exposed in the compressible delta region were known, courtesy of the full compressible boundary condition, the error of each step upwards was well defined as the values had a clear target to validate against. The mesh refinement levels followed along with the current compressible height so that the previously compressible region was simulated on a sufficiently fine grid.

2.2.2.1 Validation

The validation procedure followed the same general principals as described in Section 2.1, but the validation volume was now placed over both the compressible delta region and the static region used previously, see Figure 2.4.

The validation grid had a constant density of 10 points per $1\,cm$ increment. As the compressible delta region moved up, the number of validation points in the radial direction would remain constant while the points in the z-direction would in general follow $10i$, where $i = 5 - h$ where h is the current compresible height in centimeters.

The static validation volume remained the same over all the simulations and could therefore be used as a reliable comparison so that the two measured errors were consistent with each other. See Figure 2.4 for the placement of the static region.

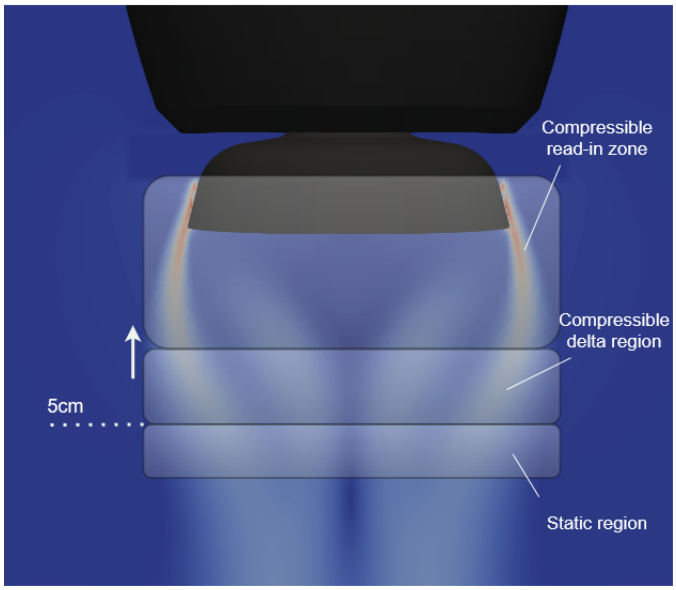

Figure 2.4: A schematic view of how the validation volumes are defined. The compressible delta region, used in the compressible height simulations continually increased in size as the height grew smaller. The static region placed under the original size of the compressible boundary condition remained static over all the simulations.

2.3 Methodology Using Particles

The particle simulation procedure was a direct continuation on the pure airflow simulations where particle injection occurred directly after the temporal convergence was reached for the airflow. This ensured both numerical and physical stability as the simulation carried on for an additional amount of time. The convergence studies for the mesh size and the Δt were repeated with particles to make sure that the updated solver, now including Equation (1.7) and the two way coupling, was converged enough. The temporal convergence study was not repeated but instead assumed to require the same amount of time as the pure airflow to reach temporal convergence. Hence the simulations would now simulate 0.04 seconds in total, the first 0.02 with pure airflow and the second 0.02 with particle injection.

2.3.1 Mesh Convergence

Prior to performing the mesh convergence two complimentary studies were made. Firstly the time step was studied so to obtain a stable CFL number for the mesh convergence. Secondly the injection rate of computational parcels were subjected to a convergence study which determined how many parcels per second, or effectively, how many parcels per time step were required to reach convergence. The total number of real particles were fixed, hence a larger parcel injection rate reduced the number of particles per parcel and thus continually reduced the effect of the parcel simplification.

2.3.1.1 Convergence of Complimentary Studies

The time step convergence was carried out on the mesh size corresponding to Case 2 in Table 2.1 which was considered converged without particles. The mesh refinements were aligned to where the particle injection occurred close to the bell and the compressible height was set to $5\,cm$ in all simulations. The fluid field was validated on the static region seen in Figure 2.4. The result of the time step convergence can be seen in Figure 2.5a, where the reference was simulation with $\Delta t = 0.025\,ms$. Using the same convergence tolerance as before the time step converges at $0.05\,ms$ which correspond to a CFL number of around 4.

The convergence of the parcel injection rate used the converged time step but otherwise the same simulation set-up as previously mentioned. The result can be seen in Figure 2.5b where an injection rate of 1e7 parcels per second reaches the convergence tolerance of 1e-3 with 1e9 parcels per second used as reference. Due to the parallelizable nature of the particle equations there was no significant increase in computational cost to use an injection rate of 1e8. Since this was a closer match to the realistic injection rate reported in 1.3.2.5 this number was used instead.

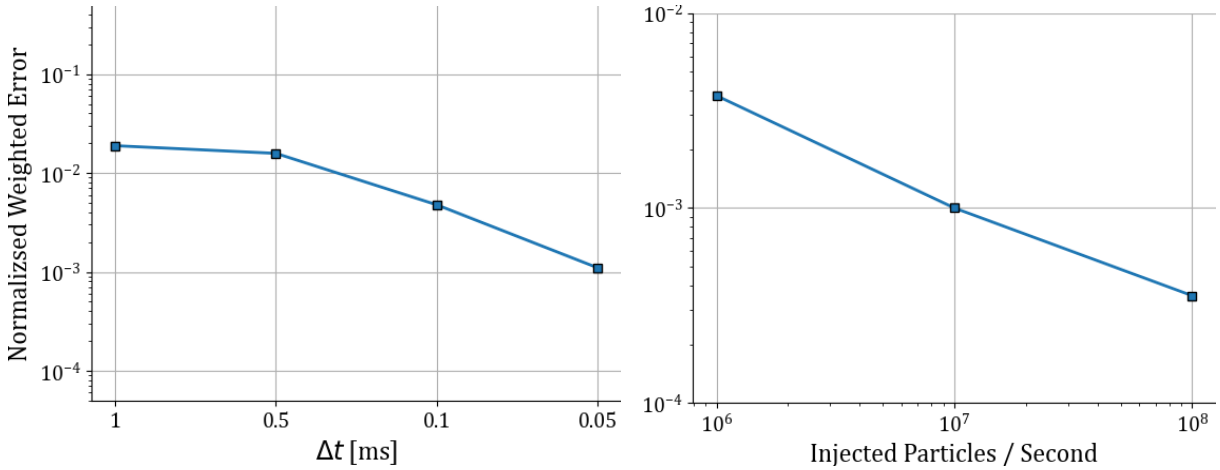

(a) Time step convergence while using particles

(b) Convergence of the number of injected parcels per second

Figure 2.5: Complimentary studies prior to the mesh convergence study for particles

2.3.1.2 Convergence of Mesh Size

The mesh convergence study was carried out using a constant CFL number of 4 and with a particle injection rate of 1e8 particles per second. Five different meshes were simulated with cell sizes corresponding to Table 2.2 and where the finest mesh size was used as the reference. The mesh structure can be seen in Figure 2.6, where the basic refinement levels are the same as without particles, but the level 4 refinement level closest to the bell covers the entire area below the bell.

Table 2.2: Details of the mesh convergence study with particles

Case	**Refinement Factor**	**Smallest Cell** [mm]	**Cell Count** (millions)	Δt [s]
1	0.75	0.833	2.5	6.67e-5
2	1	0.625	6.2	5e-5
3	1.25	0.500	13.0	4e-5
4	1.5	0.416	22.2	3.33e-5
5	1.75	0.357	35.4	2.86e-5

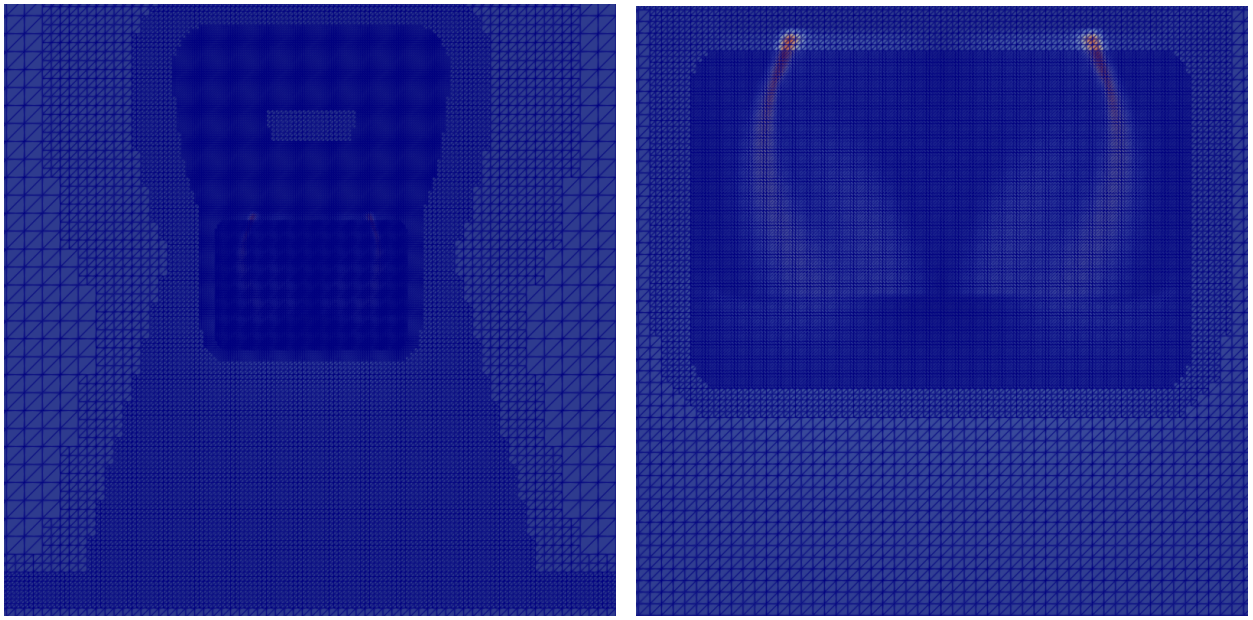

(a) Refinement increase around the bell **(b)** Mesh refinement in the validation region

Figure 2.6: Illustration of the mesh refinement structure used in the mesh convergence study with particles

The result can be seen in Figure 2.7 where the 50% refinement over the base mesh size reaches a similar error as the previous mesh study. While it does not reach the explicit convergence tolerance used thus far it is still considered sufficiently close to convergence for

the purposes in this thesis. Therefore the mesh size corresponding to Case 4 in Table 2.2 will be used for the simulations including particles going forward.

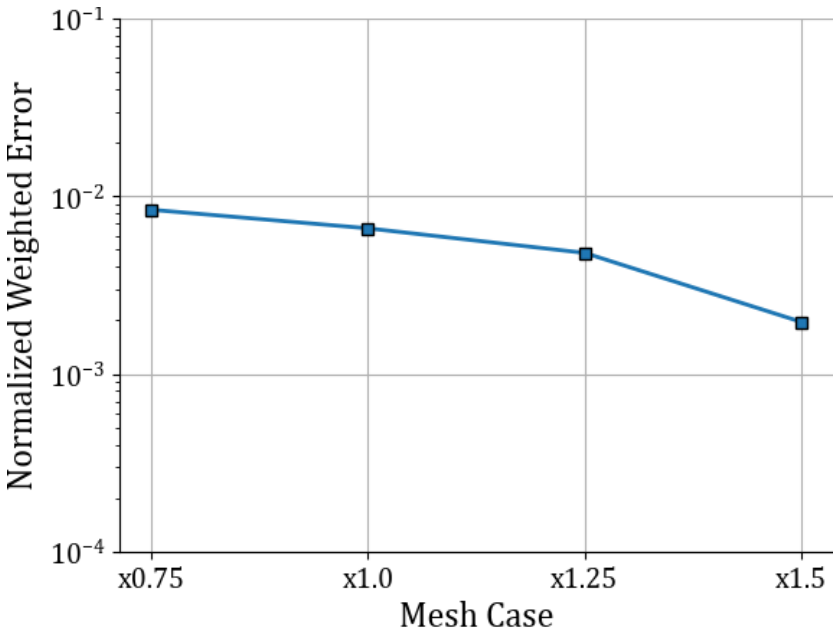

Figure 2.7: Mesh convergence study using particles

2.3.2 Compressible Height Convergence

The compressible height convergence with particles was carried out similarly to the airflow case. The finest mesh refinement now covered the entire boundary condition, as in Section 2.3.1.1, so that the particles were simulated on a sufficiently fine grid. The same two validation volumes were used as in the airflow case seen in Figure 2.4.

2.3.3 Cross Validation

The goal of the cross validation was to investigate whether a single compressible simulation could be used as the boundary condition even if the particle injection parameters varied. As mentioned in Section 1.3.2.3 *Particle Injection* there is no particle-fluid coupling occurring in the compressible boundary region, which means that this data is statically tied to a specific injection case. If the impact of the particle-fluid coupling is significant, i.e. the particle drag force is significantly different from the reference, the cross validation is expected to result in large error. The particle-fluid coupling will cause the correct boundary conditions to be too different resulting in large differences in the flow field. With a minimized, yet sufficiently accurate, compressible region found in the previously described height convergences, this study therefore evaluated the significance of the two way coupling between the phases with respect to the different injection parameters.

The cross validation was performed on three different injection parameters; slip factor, axial

velocity and dv50. The slip factor represents how much momentum loss the particles experience upon release from the rotating bell. A value of 0 means that all momentum is lost and 1 means that all momentum is preserved. The axial velocity is the velocity component in the z-direction with which the particles are injected. Note that the main velocity component for the particles on release are in the x- and y-directions due to the high angular velocity of the bell. The z-component of the velocity becomes more dominating after the release as the particles become affected by the strong shaping airflow from above. Lastly the dv50 is the mean particle size of a size distribution as the particle parcels are created.

Table 2.3: Variable injection parameters

dv50 [μm]	**Axial Velocity** [m/s]	**Slip Factor** [-]
10	10.4	0.62
25	13.9	0.82
40	17.4	1.04

In the cross validation study each of the three parameters had three associated values, seen in Table 2.3, thus resulting in 3^3 different cases. The strategy for validation was to use the case corresponding to the middle values on all parameters as the base case and subsequently cross validate on a case where only one parameter was changed. This reduced the number of validation cases to a more manageable six.

The cross validation was performed by simulating the case with its correct boundary condition at $0.5\,cm$ and $5\,cm$ compressible height and then simulated again with the boundary condition of the base case. With these three simulations three different errors were obtained, one for the incompressible simplification error, one for the cross validation error and a last one for the combined, total, error.

3

Result

The result in this thesis will, in accordance with the methodological structure, be presented in two steps where the first section covers the result of the height sweep of the pure airflow and the second section covers the fluid-particle coupled simulations where the height sweep and the cross validation were performed. As a complement in the analysis of the cross validation of the airflow there will also be paint thickness estimations presented for the same cases.

3.1 Result Without Particles

The compressible height convergence was run between 0 and 4 cm while always validating against the compressible reference data available from the 5 cm fully compressible near bell region. The error was determined over two different volumes; the variable compressible delta region as well as a static region placed directly below the 5 cm mark. The resulting normalized errors from the convergence study can be seen in Figure 3.1

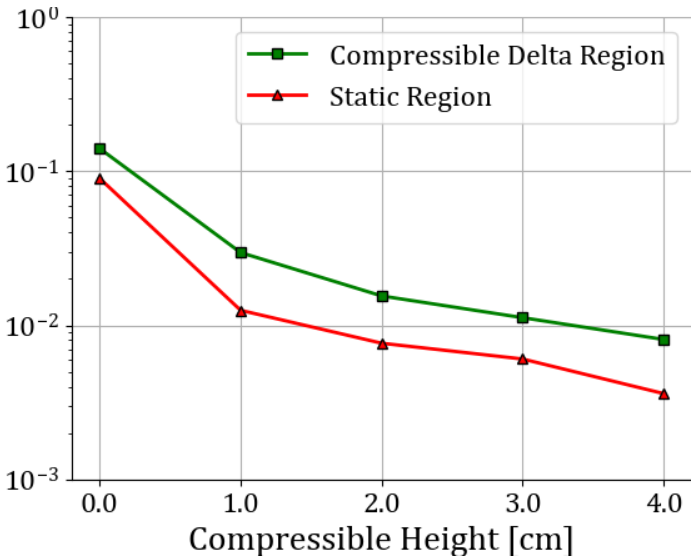

Figure 3.1: Normalized error as a function of the height of where the compressible data is read in as a boundary condition

From Figure 3.1 we can primarily see a good agreement in the trend between the two different measures, indicating that they both measure the error consistently. The error measured in the static volume however is consistently lower throughout the entire sweep. With the reservation of keeping future plots as clean as possible only the more conservative error from the compressible delta region will be used going forward.

It can further be observed in Figure 3.1 that the difference between the fully compressible near bell region and the compressible heights down to $2\,cm$ is around 1-2%. This amount of velocity deviation is small enough to be almost indistinguishable in the velocity fields, seen in Figures 3.2a and 3.2b.

At $1\,cm$ the error has grown to 3% and between 1 and $0\,cm$ there is an abrupt change in the size of the error in Figure 3.1. By observing Figure 3.2c it is possible to see a very significant change in the appearance of the flow development. Clearly the incompressible simplification diverges as the compressible heights approaches 0. This opens the question for where, in the range between 1 and $0\,cm$, an acceptable error can be obtained.

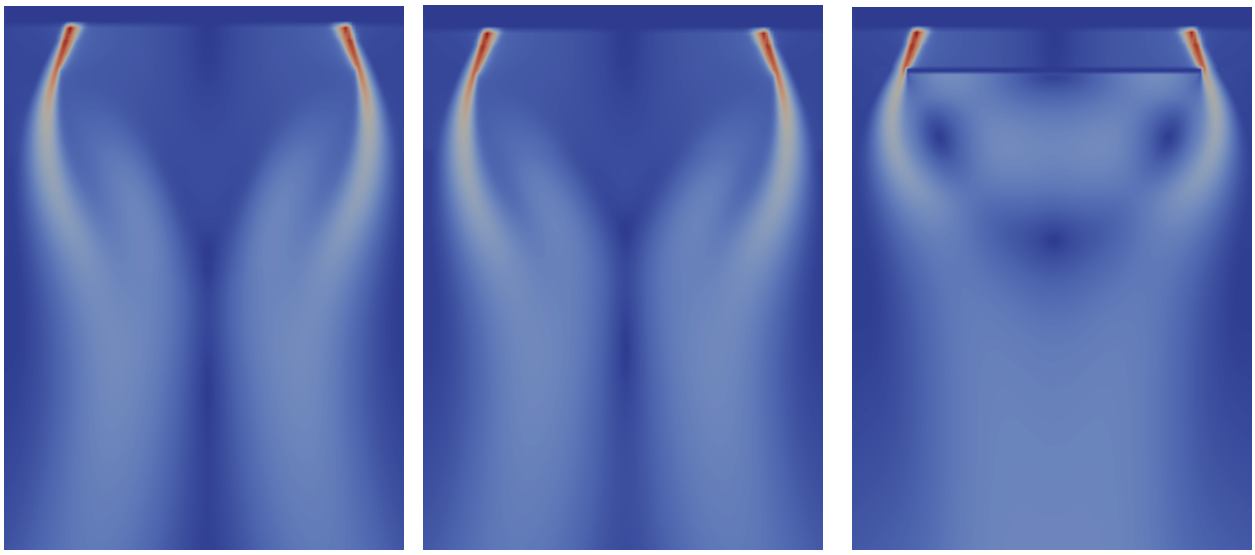

(a) $5\,cm$ **(b)** $2\,cm$ **(c)** $0\,cm$

Figure 3.2: Velocity profile of the flow field at different compressible heights

An additional step taken in the process while attempting to find the smallest compressible height was to decompose the error. The difference in the outer flow between Figures 3.2b and 3.2c, while still significant, appear to be significantly smaller than the re-circulation error. In order to be able to couple certain errors to specific regions of the flow the error was separated into and inner and an outer region which were evaluated on separate validation grids. The reason why it could be relevant to evaluate the errors in the different regions separately and differently is because the particles, in upcoming sections, are injected along the edges of the bell. The hypothesis proposed is then that the particles will not be as affected by the re-circulation error as the error in the outer flow.

The outer region was validated on a hollow cylinder where the inner radius was set to 3 *cm* which left out the entire inner region and the outer radius was set to 4.5 *cm*. The inner region was captured on a smaller, dense, cylinder with a radius just smaller than the inner radius of the hollow cylinder. The result from decomposing the error in the entire height sweep can be seen in Figure 3.3a where the outer flow is significantly more converged than the inner flow, just as expected. At 1 *cm* the error in the outer region is 1.8% while in the inner region it is 3.4%.

In Figure 3.3b the result from the attempt to find the appropriate height at which the incompressible simplification no longer diverged can be seen. Several heights were simulated between 0 and 0.5 *cm* which all saw the same traces of the diverging flow field. As the compressible height approached 0.5 *cm* the flow field converged more and more towards a more expected appearance. The flow field of 0.5 *cm* can be seen in Figure 3.4 which compares the flow field with the more expected fields from 1 and 5 *cm*. The errors for a compressible height of 0.5 *cm* are still significant in the inner region at 7%, but in the outer region the error is at 2.6%. With the motivation that the flow field at 0.5 *cm* is approaching the reference sufficiently well together with the outer flow error being relatively low, the continuation of the results are being attempted with 0.5 *cm* as the lowest possible compressible height. The tabulated errors for Figures 3.3a and 3.3b can be found in Appendix A.1.

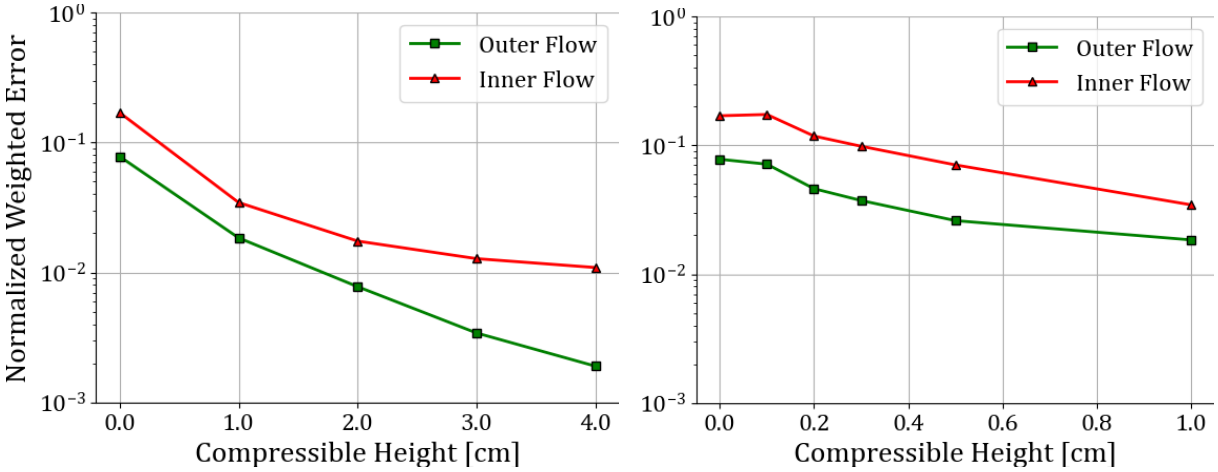

(a) Error decomposition for compressible heights between 0 and 5 *cm* in steps of 1 *cm*

(b) Error decomposition for compressible heights between 0 and 1 *cm*

Figure 3.3: Normalized error as a function of the height where the error has been decomposed into two parts representing the main outer flow and the inner recirculating flow. The errors are based on the 5 *cm* compressible height simulation as a reference.

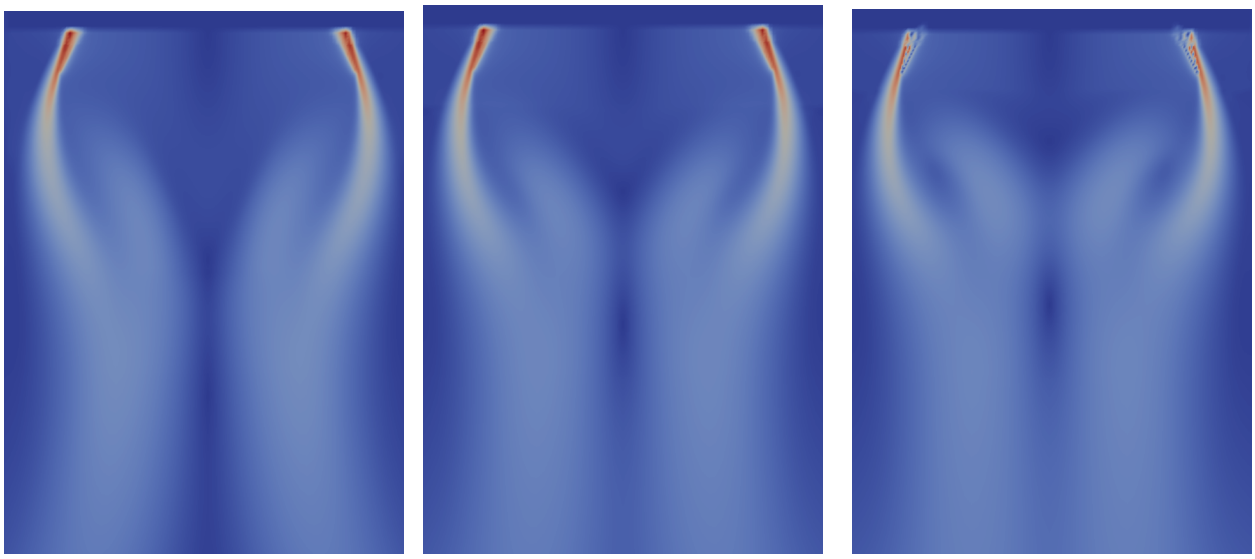

(a) 5 cm **(b)** 1 cm **(c)** 0.5 cm

Figure 3.4: Illustration of how the compressible height of 0.5 cm approaches a more expected behavior, especially of the re-circulation

3.2 Result With Particles

Just as without particles the error computed in the two different validation volumes are shown initially to ensure the validity of the measurements. From the previous section it was concluded that the airflow could not be simulated with a smaller compressible height than 0.5 cm without resulting in strange flow artifacts. Therefore the particles were not simulated on compressible heights lower than that.

The errors comparing the compressible delta region to the static region can be seen in Figure 3.5a where both regions now have a much more stable error with respect to the varying compressible heights. The corresponding airflow data at the same heights is shown as a comparison in Figure 3.5b. While the convergence error with particles do not go quite as low as without for larger compressible heights, the error at 0.5 cm becomes significantly better resolved. The addition of particles does therefore not cause any instabilities to the fluid field but reversely improves some of discrepancies seen in the pure airflow.

Again there was a good agreement between the two different validation volumes. The errors in the static region were consistently lower than in the compressible delta region, thus with the same conservative argument as before, only the compressible delta region will be shown moving forward.

The same error decomposition was performed as before where the inner and outer flows were separated to quantify where the bulk of the error was located in the flow. The error decomposition can be seen in Figure 3.6a and Figure 3.6b shows the corresponding error

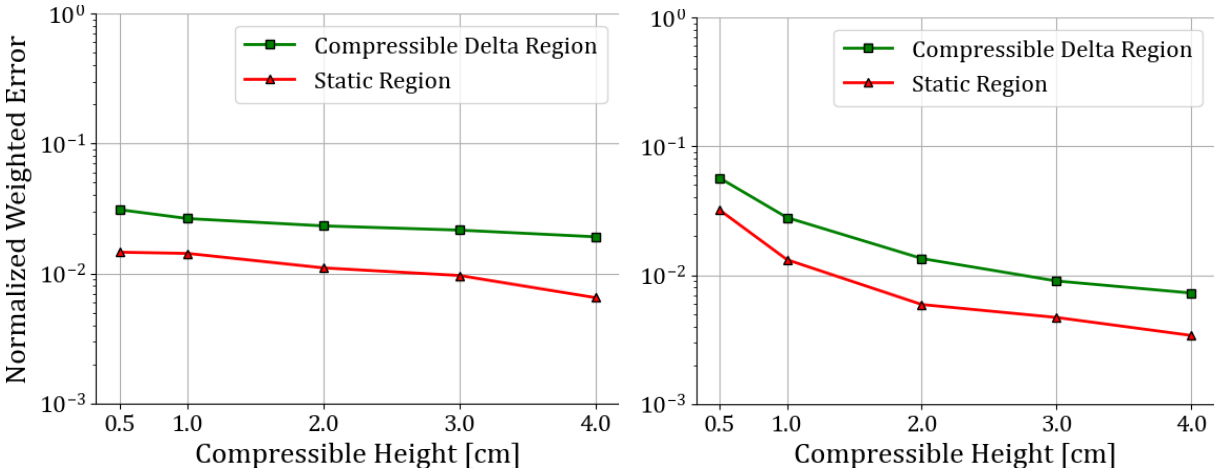

(a) With particles **(b)** Without particles

Figure 3.5: Normalized errors measured for different compressible heights comparing particle injection and airflow for both the compressible delta region and the static region

decomposition for the pure airflow. The inner and outer flow errors are very similar showing that both regions are simulated with a relatively good accuracy despite the incompressible simplification. Comparing the errors to the pure airflow simulation we can see that the inner flow converges in a relatively similar trending line, only the magnitudes of the errors at smaller compressible heights are significantly smaller. The convergence trend of the outer flow however becomes very different. The outer flow error at $0.5\,cm$ is very similar, but due to the particle injection and the incompressible simplification it becomes harder to accurately solve the outer region and the error remain more or less the same for all compressible heights. The reason why the inner region sees such large decreases in the flow error could be an artifact of the large amount of extra momentum which is now inserted into the domain. The amount of two way coupling that the particles provide on the development of the fluid field seem to stabilize it around some given mode whose effects are more prominent than than the incompressible simplification. The inner flow error at $0.5\,cm$ is 3.7% with particles compared to the 7% without as reported earlier. The outer flow errors are 2.3% and 2.6% for with and without particles respectively. Since the errors decreased with particle injection to relatively low values, it was deemed appropriate to consider $0.5\,cm$ as the converged compressible height and perform the upcoming studies using this value. The tabulated errors for the height sweep can be found in Appendix A.2.

3.2.1 Cross Validation

The cross validation of the particle injection parameters was performed by varying a single injection parameter at a time. The injection parameters were first used to simulate the case where the boundary condition and particle settings matched with the same injection case, both at $0.5\,cm$ and $5\,cm$. The injection parameters were then used to simulate the case where

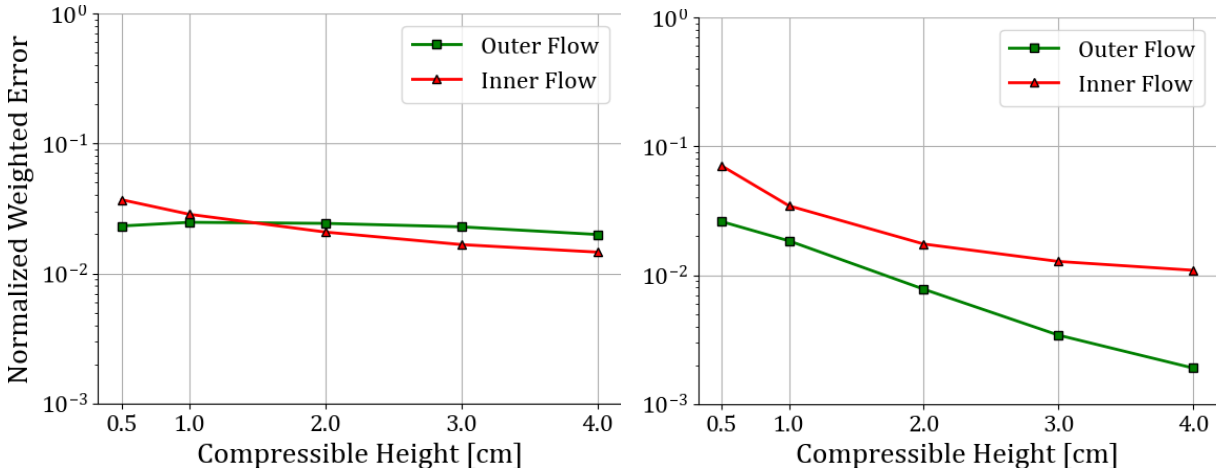

(a) With particles **(b)** Without particles

Figure 3.6: Decomposed normalized errors measured for different compressible heights comparing the particle simulations with pure airflow for the compressible delta region

the boundary condition did not match the injection case at 0.5 *cm*. By simulating these three cases three different errors were obtained; the error from the incompressible simplificaton of the near-bell region up to 0.5 *cm* from the injection point, the error from the injection parameter crossing and lastly the total, combined, error when applying both simplifications. The injection parameters used as the base case for the crossings - the use of which described in Section 2.3.3, was the same case used in Section 3.2.

Since the cross validation was performed at 0.5 *cm* instead of a more ideal 0 *cm*, it had 0.5 *cm* of space where the two-way coupling between fluid and particles were incorrect. The error from the parameter crossing therefore shows a measure of how much the two way coupling matters in this smaller region for that specified injection parameter.

Tabulated errors for all data points can be found in Appendix A.3 and the flow fields associated with the different stages of simplification can be found in Appendix B.

3.2.1.1 Error from Incompressible Simplification

The error from the incompressible simplification of the near bell region is presented first. This is a throwback to the height sweeps made previously but where the errors are now computed over the different injection cases for the given compressible height of 0.5 *cm*.

The errors for all three injection parameters can be seen in Figure 3.7. Important to note is that the errors in any given plot stems from only changing that specific injection parameter. The middle of the three values associated with each injection parameter is the base case and correspond to the errors found in Section 3.2.

By firstly studying Figure 3.7a showing dv50, which is the mean value of the particle size

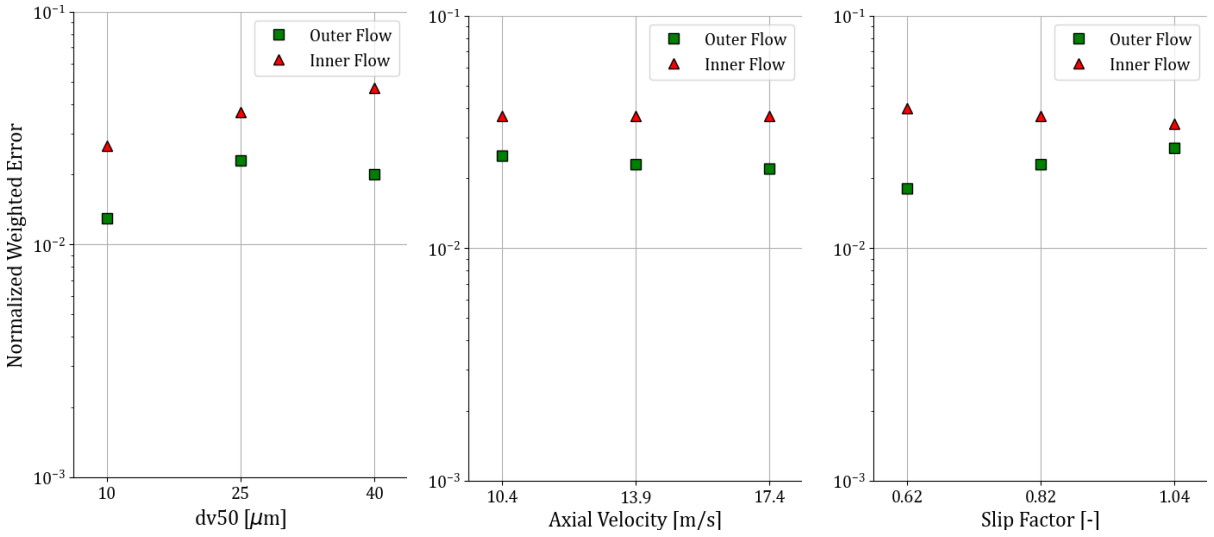

(a) dv50 **(b)** Axial velocity **(c)** Slip factor

Figure 3.7: Visualization of the errors from the incompressible simplification of the near-bell up to 0.5 cm for the three different injection parameters

distribution, the inner flow error increases linearly with an increasing particle mean size from 2.7% at 10 μm to 4.7% at 40 μm. The outer flow has significantly smaller errors, 1.3% and 2.0% respectively, and does not as clearly show the same trend with increasing errors for increasing particle sizes.

By changing the axial veloicity, which is the z-component of the injection velocity, the error from the incompressible simplification is impacted to an almost insignificant degree, as seen in Figure 3.7b. The inner flow errors remains constant at 3.7% as the axial velocity changes and the outer flow error decreases from 2.5% to 2.2% with increasing axial velocity.

The slip velocity in Figure 3.7c shows that the error from the incompressible simplification increases for the outer flow as the slip factor increases while the reverse to true for the inner flow. This result should make some intuitive sense since a larger slip velocity preserves the momentum of the particles to a larger degree, a momentum which is primarily directed radially - in the x-y-directions, and should thus result in fewer particles ending up in the re-circulation region on average.

3.2.1.2 Error from Parameter Crossing

Next the errors associated with the parameter crossings are presented. They were obtained by comparing the simulation using a 0.5 cm compressible height as the injection parameters matched with the same height but where the injection parameters were miss matched. The result of the cross validation can be seen in Figure 3.8 for all three free parameters. There will no longer be any data presented for the base case since the errors are relative to that case.

Starting with dv50 in Figure 3.8a it can be seen that the inner region was significantly more impacted by the incorrect two-way coupling resulting in a normalized weighted error of 2.9% and 2.0% for 10 μm and 40 μm respectively. The outer region was not as affected with errors of 1.1% and 0.7% respectively.

Next it can be observed that the axial velocity is highly resistant to the inconsistency of the two-way coupling near the bell. The maximum errors measured between the reference and the cross set-up was 0.3%, rendering the two simulations indistinguishable from one another. Lastly, the slip factor has errors which lies in between the two previous parameters. The errors of the inner flow is around 1% and the outer flow between 0.6% and 0.7% indicating a very small impact in the two-way coupling as well.

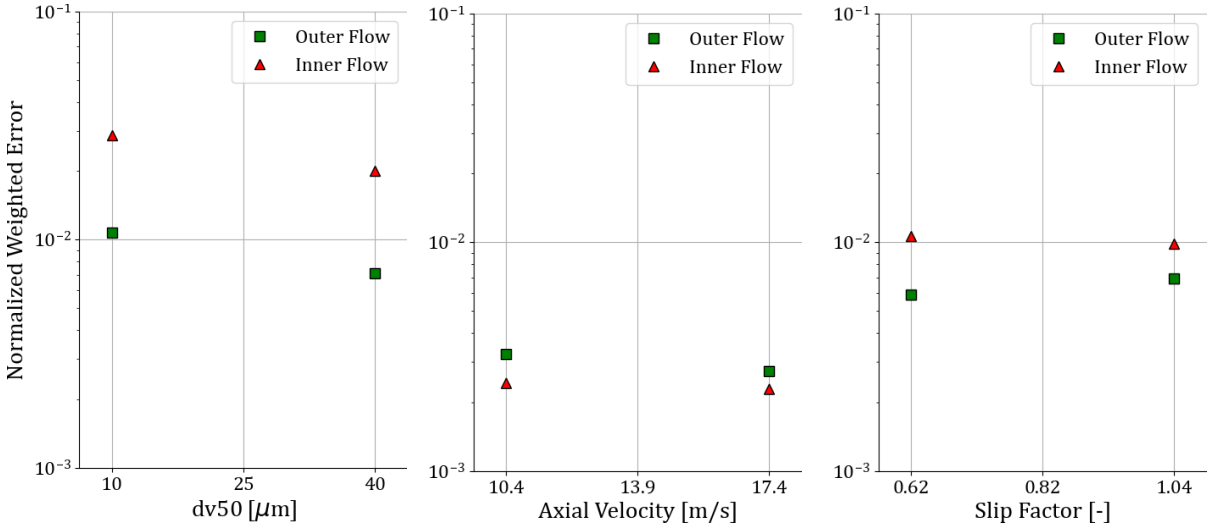

(a) dv50 **(b)** Axial velocity **(c)** Slip factor

Figure 3.8: Visualization of the cross validation result for the three different injection parameters

3.2.1.3 Total Error

Lastly the total error, i.e. the combination of the two errors above, is presented. While the total errors are a combination of the two previous errors it is not trivially going to be a super position of the two. Since the errors are computed in absolute and scalar terms they do not specify a sign or direction of the error, which is why the total error may end up smaller, or larger, than the sum of the components.

Observing the errors for dv50 in Figure 3.9a this is exactly what happens at 40 μm where the inner flow error is at 3.3% after having been 4.7% based on the incompressible simplification. In Figure B.2 it can be seen that the flow field in the inner region changes significantly after the incompressible simplification (Figure B.2b) and using the crossed injection parameter results in a similar but, on the whole, less erroneous re-circulation (Figure B.2c). Oppositely

when dv50 is reduced to 10 μm the total error in the inner region increases due to the cross validation to 5% after being around 3% before. The difference in flow development can be seen in Figure B.1 where it becomes clear how each simplification gives a re-circulation pattern more different compared to the 5 cm reference. Observing the outer flow however the errors are at, or just below, 2% which is in fact smaller than the outer flow errors seen in Sections 3.1 and 3.2.

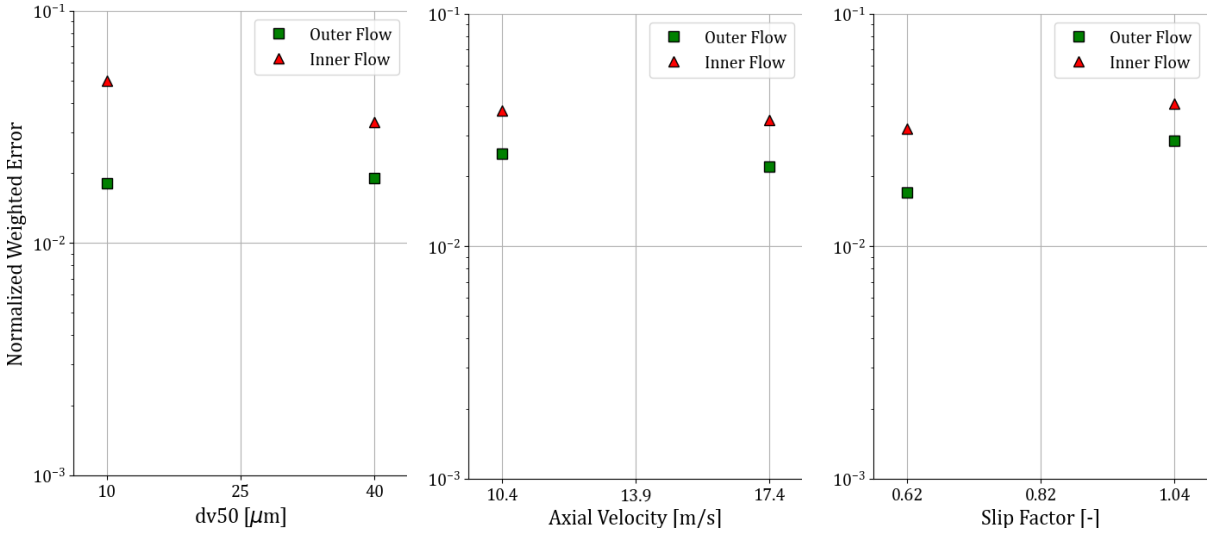

(a) dv50 **(b)** Axial velocity **(c)** Slip factor

Figure 3.9: Visualization of the total error, including both the error for the incompressible simplification up to 0.5 cm and the injection parameter miss match, for the three different injection parameters

When it comes to the axial velocity in Figure 3.9b the total errors are more or less equivalent to the incompressible simplification error mentioned in Section 3.2.1.1 which is expected since the impact of the parameter crossing was so marginal in Figure 3.8b. The flow fields can be observed in Figures B.3 and B.4 which illustrates the larger errors in the re-circulation region due to the incompressible simplification but a more or less an identical flow field between the two simplifications.

Lastly, the total error after changing the slip factor sees relatively large changes in the inner flow error compared to the errors from just the incompressible simplification. For a slip factor of 0.62 the error decreases from 4% down to 3.2% while for 1.04 it increases from 3.4% to 4.1%. Even though the re-circulation errors changes in the cross validation it is difficult to note any differences in the flow fields in Figures B.5 and B.6. The differences are therefore mainly related to magnitudes rather than a fundamental change in flow behavior. The outer flow errors are almost identical to the errors from the incompressible simplification at 1.8% and 2.8% respectively.

3.2.2 Paint Thickness Error

The focus in this thesis has been to study the differences in the airflow field to validate the two different proposed simplifications. This is an indirect way of estimating how well the final paint result will turn out since it does not account for the paint distribution impacting on the surface. Getting a more representative view of the validity of the result generally involves obtaining the paint thickness distributions through the kernel density method briefly covered in Section 1.3.2.5.

Early results of the paint thickness estimations with respect to the simplifications, showing an outlook of the future studies in this subject, will now be presented. It will also be further discussed in Chapter 4. To obtain the paint thickness estimations a coarser simulation was run for the larger scales using a boundary constructed by time averaging and combining a compressible simulation between $-2\,cm$ and $0.5\,cm$ and an incompressible simulation from $0.5\,cm$ down to $5\,cm$. The coarser simulation kept track of the paint particle impacts on the surface and constructed a thickness estimation using the Kernel density method. The results of the simplifications are compared to the fully compressible near-bell region for which the boundary condition did not contain any part of the IBOFlow simulation.

When the paint thickness is optimized it is compared to experimental data, as mentioned in Section 1.3.2.3. Changing some of the injection parameters will make the paint distribution of the simulations either more or less similar to the experimental data and where the aim of the optimization is the minimize the differences. The experimentally obtained paint thicknesses come from an ERBS applicator drawn over a segment in a straight line. Along the segment the paint thickness is measured at three different perpendicular lines spanning $400\,mm$ to each side of the ERBS applicator. For a given set of physical parameters - such as the velocity of the shaping airflow or the paint flow rate, the experimental tests result in Figure 3.10. The mean thickness is plotted together with the maximum and minimum measured values which in relation creates a rough variance associated with the experiment. The large differences in the noise seen for the outer rims of the paint distribution are ignored when determining the variance, instead the focus lies with the region between approximately $-100\,mm$ and $100\,mm$. From Figure 3.10 it can be determined that the largest positive measurement error was $4.83\,\mu m$ and the largest negative measurement error was $3.90\,\mu m$. This variance can in some sense be used as a guide for the level of uncertainty regarding the experimental measurements and any paint thickness deviations from the different simplifications which is still within this range can be considered as acceptable.

Throughout this section the comparisons are made between the same cases as previously; the fully compressible near-bell region, the incompressible simplification up to $0.5\,cm$ as well as the total error combining the incompressible simplification and the cross validation. To distinguish the cross validation error from the total error one only needs to compare the difference between the total error and the incompressible simplification.

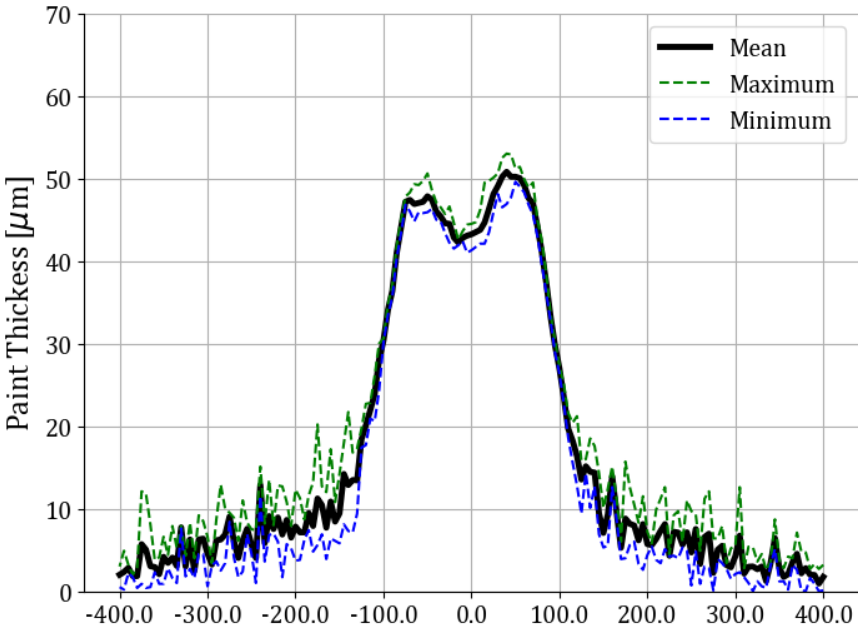

Figure 3.10: Experimentally obtained paint thickness. It includes the maximum and minimum measurement values as well as the mean of all measurements.

3.2.2.1 dv50

The estimations of the paint thickness for the dv50 can be observed in Figures 3.11 and 3.12. A dv50 of 10 μm, seen in Figure 3.11, results is large differences in the paint thickness estimations. Both simplifications increases the differences to a great degree separately, where the incompressible simplification has differences on the order of 5 μm and the cross validation simplification accumulates the total differences to be on the order of 10 μm compared to the fully compressible near-bell reference. The incompressible simplification is on the boarder of that the experimental variance allows and the total error overshoots this signigicantly. The overall trend of the differnet simplifications corroborates quite well with what was reported in Section 3.2.1.3 where the inner flow error was reported to have increased from 3% to 5% due to the cross validation simplification.

For a dv50 at 40μm in Figure 3.12 the resulting differences in the estimations from both the incompressible simplification and the cross validation were on the order of one micrometer. This is a large difference compared with the lowered value of dv50 and intuitively an increase in dv50 should correspond to somewhat similar errors as for the lower. In the analysis of the airflow that is what was ultimately found but something unexpected happens here where the airflow result and the particle tracking become significantly decoupled. This is discussed to some extent in Section 4.3

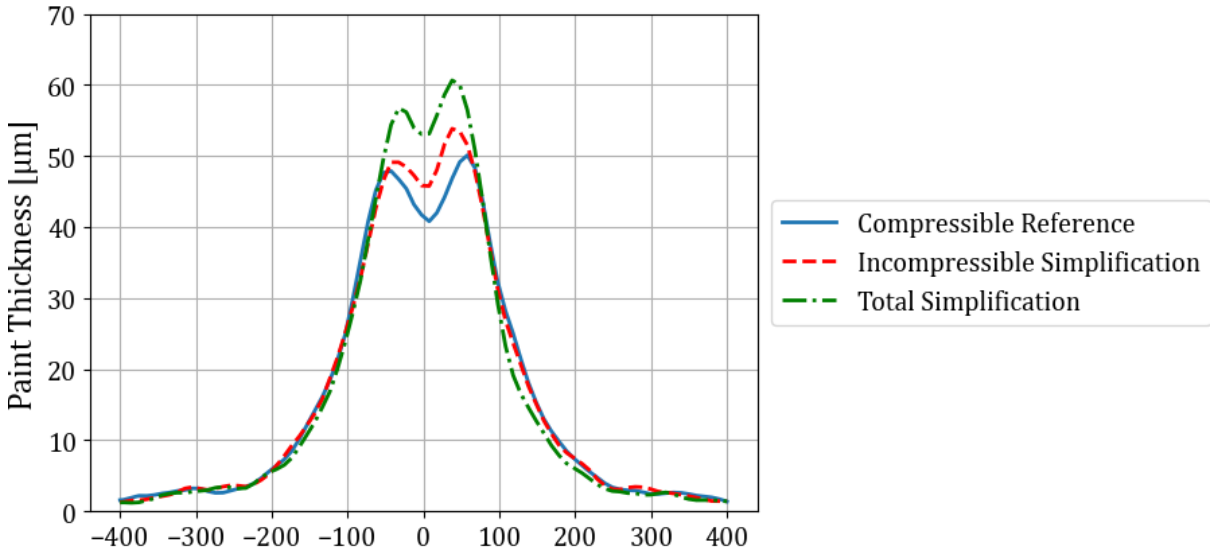

Figure 3.11: Paint thickness estimations for dv50 at $10\mu m$ comparing the different simplifications.

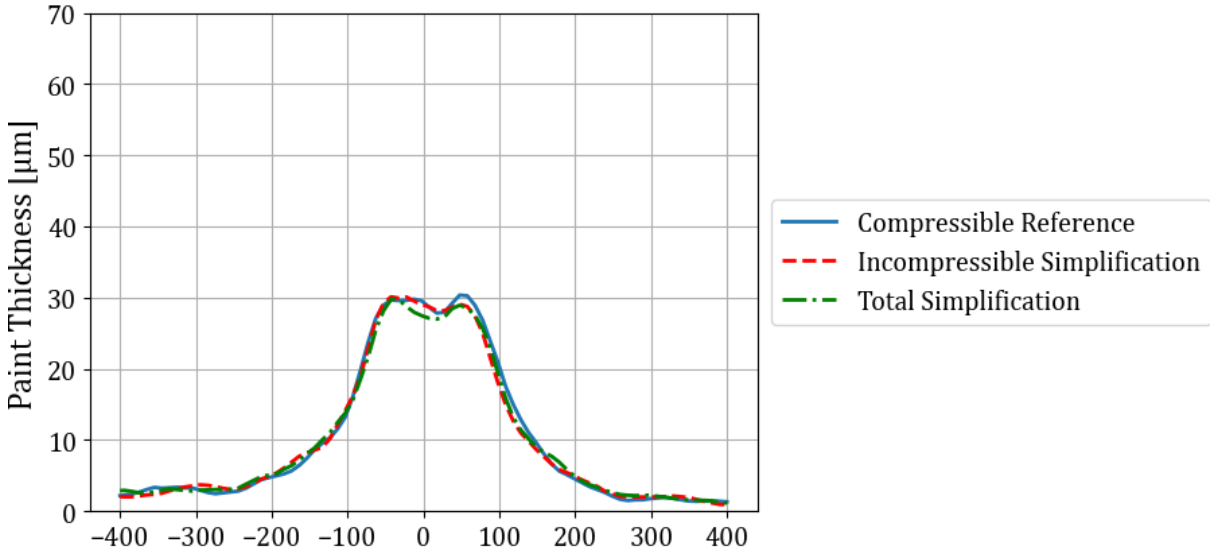

Figure 3.12: Paint thickness estimations for dv50 at $40\mu m$ comparing the different simplifications.

3.2.2.2 Axial Velocity

The paint thickness estimations for a variable axial velocity can be seen in Figures 3.13 and 3.14. Figure 3.13 show the thickness differences between the different simplifications with a lowered axial velocity compared to the base injection case. The impact of the cross validation is very small, similar to what was found in Section 3.2.1.2, with a maximum difference on the order of a single micrometer. Most of the errors originate from the incompressible simplification with errors on the order of five micrometers which is on par with the experimental variance.

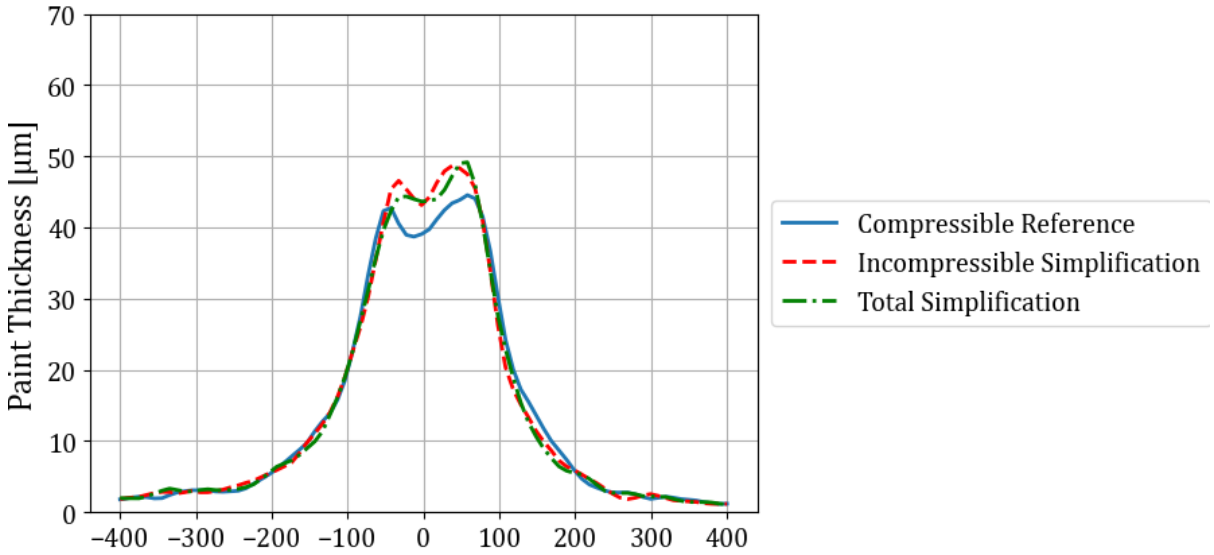

Figure 3.13: Paint thickness estimations for axial velocity of $10.4\,m/s$ comparing the different simplifications.

A similar trend is seen as the axial is increased with respect to the base injection case. The impact of the cross validation on the paint thickness estimation is very small while the incompressible simplification errors becomes more significant on the order of five micrometers which again is on par with the experimental variance.

3.2.2.3 Slip Factor

Lastly a paint thickness estimation was made for the slip factor where the result of lowering it to 0.62 can be seen in Figure 3.15. The thickness estimations show a relatively good agreement across the different simplifications and where the total simplification thickness is closer to the $5\,cm$ reference case than just the incompressible simplification. The magntiude of the thickness differences are on the order of a couple of micrometers and therefore within the rage of the experimental variance. The trend of this result is in agreement with the reduction of the total error in the airflow field reported in Section 3.2.1.3.

An increase in the slip factor, seen in Figure 3.16, shows that again the the cross validation part of the simplification has a much smaller impact than the incompressible simplification.

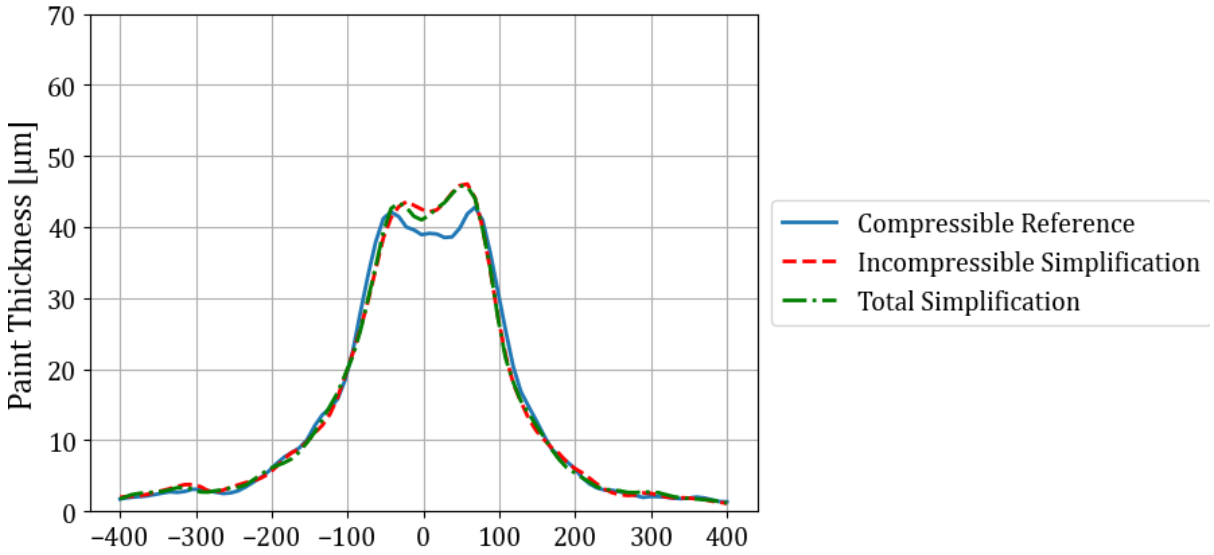

Figure 3.14: Paint thickness estimations for axial velocity of $17.4\,m/s$ comparing the different simplifications.

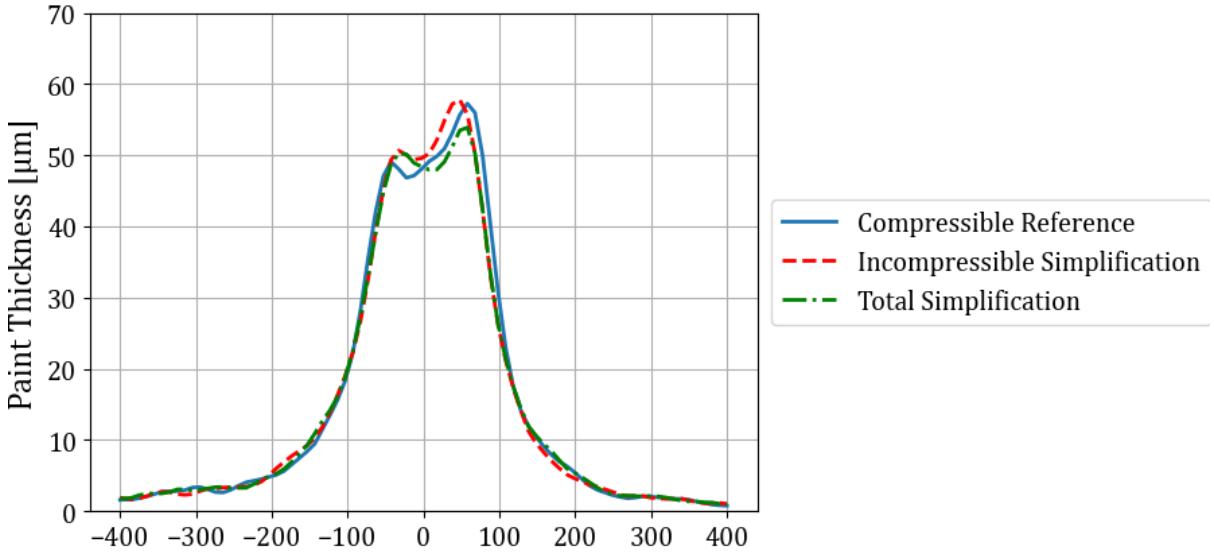

Figure 3.15: Paint thickness estimations using a slip factor of 0.62 comparing the different simplifications.

The total error becomes further from the compressible reference, but not to the same degree the incompressible simplification deviates from the reference where the differece is on the order of 5 micrometers. This result also corroborates well with what was found in the analysis of the airflow field where the total errors increased after applying both simplifications.

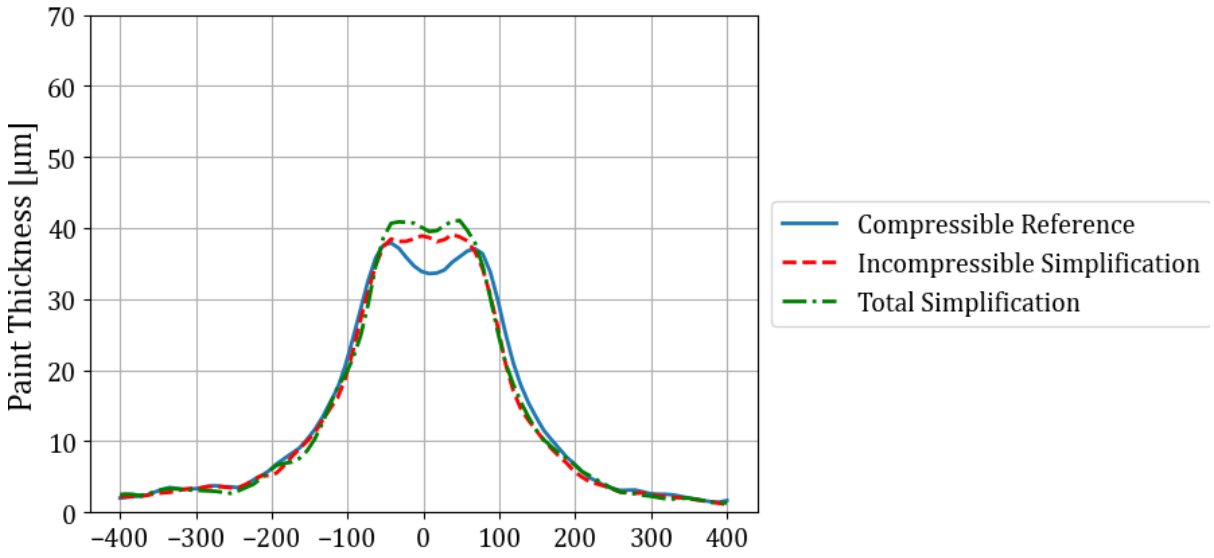

Figure 3.16: Paint thickness estimations using a slip factor of 1.04 comparing the different simplifications.

4

Discussion

The following chapter will cover some discussion topics touching on uncertainties associated with the result or the methodological choices which in some way needs to be addressed. Some of the uncertainties will additionally be quantified concretely but since they were investigated in a post-result time frame the magnitudes of the uncertainties need to be inferred on the results presented in Chapter 3. The following chapter will additionally cover a brief discussion regarding the two different methods of validation seen in the previous chapter and whether it is possible to couple the results in any way.

4.1 Uncertainty in the Weighted Error

In Section 2.1.1 *Validation Metric* the weighted average error was defined. The error fundamentally consisted of a velocity difference magnitude, with respect to some reference, which was weighted by an expression to signify the relative importance of that difference. This expression, defined in Equation (2.2), took the magnitude of the velocity difference and normalized it on the non-reference velocity magnitude of that point. With the clarity of hindsight, the velocity which normalized the weights should have been the reference velocity. Since the reference usually was a constant over many different simulations this would have provided a more stable overall weight. The expected stability issues would be most prominent where the flow field development differed significantly with respect to the reference. In examples such as Figure 3.2, which illustrates the large difference in flow field development as the compressible height approached $0\,cm$, using the non-reference velocities as the normalizing factor would in fact dampen the overall error. This stems from the fact that large areas in the non-reference re-circulation flow had order of magnitudes larger velocities than the reference and therefore reduced the size of the weights in these regions. In flow fields where the reference and the non-reference flow fields were more similar - corresponding to the most cases in this thesis, the dampening effects would only be very small. Especially in the outer region were the flow was mostly very uniform over the different simulations. An argument can be made, with respect to the above discussion, that the re-circulation errors in the inner flow - which did constitute a relatively large change in the flow development, were somewhat under estimated in this thesis.

4.2 Uncertainty in Parcel Injection Rate

The convergence of the injection rate of computational parcels in Section 2.3.1.1 was performed on a compressible height of $5\,cm$ and validated on the $1\,cm$ large region below the compressible boundary condition. As mentioned in that section the convergence occurred at 1e7 parcels per second but due to the insignificant increase in computational cost using 1e8 parcels per second, that injection rate was used instead.

The effect of the particle-fluid coupling is assumed to be largest closer to the injection where the particles are mostly traveling orthogonal to the fluid flow, but if the simulation occurs on a domain with a large static boundary condition this coupling will never occur. The choice of compressible height therefore carries a certain amount of uncertainty for the validity of the result of the convergence study. A quick validation comparing an injection rate of 1e8 to 1e9 was therefore performed to quantify the potential error of this methodological decision. The study showed that the difference of injecting 1e8 parcels and 1e9 parcels per second using a compressible height of $0.5\,cm$ was insignificant. The measured error amounted to 1.1e-3 which was the commonly used convergence tolerance in the methodology of this thesis. It can therefore be concluded that a tenfold increase in parcel injection rate from 1e8 to 1e9 does not affect the fluid field to any significant degree even if the compressible boundary condition is reduced to $0.5\,cm$ and the validity of the proposed results in Chapter 3 holds well with regards to this variable.

4.3 Field- and Thickness Error Coupling

The result in Chapter 3 presented two different views of the validity of the proposed simplifications, one using the velocity differences in the airflow field and one measuring the difference in the paint thickness distributions. This part of the discussion shall try and determine whether the errors using the airflow field could be used as a representative proxy for the final thickness distributions and if any general trends can be found between the two different measures.

The results for the thickness estimations seen in Section 3.2.2 reported some general agreements with the analysis of the flow fields. In fact, if the result obtained from the dv50 is disregarded for a moment, the two different validation methods correspond relatively well with each other. The cross validation errors for the axial velocity is the smallest in both methods and also more or less insignificant, which is expected since the axial velocity does not impact the particle drag force and thereby the two-way coupling. The cross validation errors for the slip factor are larger than for axial velocity yet still not largely significant. The most significant errors for both injection parameters originates from the incompressible simplification which is also confirmed by both validation methods. Even details such as the lowered slip factor, which becomes closer to the reference after the incompressible

simplification, is clearly visible in both methods.

The result for the dv50 becomes somewhat harder to explain in a similar manner as for the other injection parameters. The incompressible simplification error while studying the airflow field for a lower dv50 has the smallest errors of any parameter value and yet the paint thickness error is one of the most significant. The higher dv50 has significantly larger errors for the incompressible simplification in the flow field, but insignificant differences in the paint thickness estimation.

The effects of cross validation is expected to be very high for dv50 since the particle size is the most significant factor to the drag force from Equation (1.7). For a lower dv50 this is true since both the airflow error and the paint thickness error is by far the largest of any other parameter. The larger value of dv50 however again show a significant difference between the two validation methods. The paint thickness estimation show a negligible impact from the cross validation which goes against what is measured in the airflow and what intuition tells us. It is possible that the larger particle sizes associated with an increased dv50 cause lead to a high over spray which in combination to the elimination of the electrostatic solver drove much of the paint away from the measurement area in the paint thickness estimations. This would explain why the estimation has such low thicknesses compared to the lowered dv50 and why that is seen even for the fully compressible reference. Now the analysis of the airflow still showed relatively significant errors based on the increase of dv50. One explanation for this is that the airflow was mostly impacted by the erroneous compressible boundary condition which it read in and not by the two way coupling. The two way coupling was relatively low since the particles tended to fly out more and thereby result in this clear decoupling we could see between what the particle data tells us through the paint thickness and what the airflow analysis tells us.

On the whole it could therefore, with respect to the above discussion, be problematic to use the airflow field errors as a proxy for the paint thickness estimations. While it works relatively well for two of the injection parameters it sometimes behaves counter intuitive to the other. It is also in general difficult to predict paint thickness errors based on the errors in the airflow, where similar errors between different injection parameters could result in larger differences in the paint thickness esitmations. The error decomposition introduced in Chapter 3 in association with the airflow errors is also somewhat dubious when comparing to the paint thickness estimations. The hypothesis that the outer flow should be the dominating factor for particle trajectories cannot be enforced by much evidence presented in this thesis. The outer and inner flow most commonly trend together with the outer flow mostly having smaller errors and therefore it is difficult to be able to distinguish if any region has a larger impact then another. It should also be noted that the degree to which any region impacts may also be dependent on how the injection parameter affects particle momentum for example. Parameters which increase momentum generally gets fewer particles in the inner region and may therefore be more dependent on the outer flow and vice versa. It should lastly be

mentioned that since this thesis excluded the electrostatic effects, the result may have been significantly different with respect to the behavior of the different injection parameters which could normally be expected from an ERBS applicator. A study which builds on the results in this thesis and additionally includes electrostatic forces is therefore left as a viable next step for future work.

5

Conclusions

This thesis has investigated how an incompressible simplification of a previously compressibly simulated near-bell region for an industrial ERBS applicator can be utilized. The thesis did, in order to drive down complexity, not include the electrostatic effects of the ERBS - something that therefore maximized the effects of particle-fluid coupling. The incompressible simplification was performed for a pure airflow as well as for a particle-fluid coupled simulation. The thesis also investigated the particle-fluid coupling with respect to different injection parameters and how well a single injection parameter for the compressible boundary condition could be used uniformly across a wide range of different injection parameters in the incompressible simplification. All investigations were made in accordance with Section 1.8 *Problem Statements* and the CFD software used was the in-house developed product by Fraunhofer Chalmers Centre called IBOFlow.

The main validation of the simulations used a weighted error based on the fluid cell velocities where the weights were determined to represent the relative significance of the velocity difference with respect to a reference. The weighted error was normalized on the maximum velocity of the domain, resulting in errors which could be described in terms of percentages.

From the results presented in Chapter 3 clear conclusions can be drawn. Based on simulating a pure airflow it was determined that the size of the compressible boundary condition could be reduced so that it spans from $-2\,cm$ to $0.5\,cm$, instead of $5\,cm$, in the z-direction and symmetrically between -4.75 and $4.75\,cm$ in the x-y-directions. At this height the most extreme forms of the diverging flow field which appeared close to the bell as an artifact of the incompressible simplification was no longer present. The errors associated with this degree of simplification was 5.6% overall, or 2.6% and 7.0% if the errors were decomposed into an outer and inner region respectively. The addition of dispersed particles and an associated two-way coupling between the fluid and dispersed phase significantly improved the errors of the incompressible simplification closer to the rotating bell. The overall error was reduced to 3.3% or 2.3% and 3.7% for the decomposed outer and inner regions respectively.

Subjecting injection cases to a parameter crossing where the IBOFlow simulation and the remaining compressible boundary condition utilized different injection parameters had a varying impact. With one injection case as a base the parameter which was most impacted

by this miss match was the mean particle size - dv50, especially for the inner flow where the errors solely based on the miss match was 2.9% and 2.0%. The outer flow however had errors of around 1%. The slip factor and especially the axial velocity were not as sensitive as the dv50 with errors between 0.3% and 1%.

The total error, obtained from combining the two different simplifications proposed in this thesis, concluded that errors in the outer region were mostly stable around 2%. The injection parameter with the smallest outer flow error on average was the dv50 with 1.8% and 1.9%. The parameter which had the largest outer flow error, at 2.8%, was the slip factor as it was increased to 1.04. A slip factor this high however should be taken with a grain of salt as values closer to and especially above one are not physically feasible. The total errors in the inner regions were most commonly between 3 and 4% with the outlier of 5% for one of the dv50 cases.

Lastly, paint thickness estimations were simulated for all the cases studied in the cross validation which in effect coupled the associated errors in the airflow field to actual paint distribution errors. The result showed relatively good agreement between the two validation methods for the axial velocity and the slip factor where general trends and relative sizes of errors could be observed in both methods. It was found that the effects of the cross validation in general had to low impact on the total errors and that the main source of differences was due to the incompressible simplification. For dv50, a lower degree of agreement was found between the methods where the paint thickness estimation reported both the lowest and highest errors for any of the parameters. This result was in opposition to the errors in the airflow and somewhat to the general intuition.

The validity of using the errors in the airflow as a reliable proxy for the errors in the paint thickness distributions is therefore relatively low. Equivalent or very similar errors based on the airflow field can diverge in how well the paint thickness distributions turn out. It is possible that there is a connection to which injection parameter is used and results may change by introducing the electrostatic effects.

References

[1] F. Edelvik, A. Mark, N. Karlsson, T. Johnson, and J.S Carlson. "Math-Based Algorithms and Software for Virtual Product Realization Implemented in Automotive Paint Shops". In: Math for Digital Factory, L. Ghezzi, D.Hömberg, Ch.Landry (eds.), Springer Verlag, Berlin, pp. 231-251 (2017).

[2] Karina Puurunen Roger Gottleben Adriana Tellez and Henna Poikolainen. "Climate impact of a passenger car in Sweden - Total CO2 equivalent emissions of a passenger car in Sweden from a life cycle perspective". In: Energiforsk 724 (2021). URL: https://energiforsk.se/media/29585/climate-impact-of-a-passenger-car-in-sweden-energiforskrapport-2021-724.pdf.

[3] Sadegh Poozesh, Nelson Akafuah, and Kozo Saito. "Effects of automotive paint spray technology on the paint transfer efficiency – a review". In: Proceedings of the Institution of Mechanical Engineers, Part D: Journal of Automobile Engineering 232.2 (2018), pp. 282–301. DOI: 10.1177/0954407017695159. eprint: https://doi.org/10.1177/0954407017695159. URL: https://doi.org/10.1177/0954407017695159.

[4] Kotaro Yasumura, Yasuhiro Saito, Masakazu Shoji, Yohsuke Matsushita, Hideyuki Aoki, Takatoshi Miura, Shin Ogasawara, Masatoshi Daikoku, Minori Shirota, and Takao Inamura. "Development of quantitative evaluation method for droplet behavior with high speed rotary bell-cup atomizer". English. In: Kagaku Kogaku Ronbunshu 37.4 (Aug. 2011), pp. 296–304. ISSN: 0386-216X. DOI: 10.1252/kakoronbunshu.37.296.

[5] Kevin Ellwood, Janice Tardiff, and Seyed Alaie. "A simplified analysis method for correlating rotary atomizer performance on droplet size and coating appearance." In: Journal of Coatings Technology & Research 11.3 (2014), pp. 303–309. ISSN: 19459645. URL: https://search.ebscohost.com/login.aspx?direct=true&db=edb&AN=95798958&site=eds-live&scope=site&authtype=guest&custid=s3911979&groupid=main&profile=eds.

[6] Mohammad-Reza Pendar and José Carlos Páscoa. "Atomization and spray characteristics around an ERBS using various operational models and conditions: numerical investigation". In: International Journal of Heat and Mass Transfer 161 (2020), p. 120243. ISSN: 0017-9310. DOI: https://doi.org/10.1016/j.ijheatmasstransfer.2020.120243. URL: https://www.sciencedirect.com/science/article/pii/S0017931020331793.

[7] Mohammad-Reza Pendar and José Carlos Páscoa. “Numerical modeling of electrostatic spray painting transfer processes in rotary bell cup for automotive painting”. In: International Journal of Heat and Fluid Flow 80 (2019), p. 108499. ISSN: 0142-727X. DOI: https://doi.org/10.1016/j.ijheatfluidflow.2019.108499. URL: https://www.sciencedirect.com/science/article/pii/S0142727X19305995.

[8] A. Mark, B. Andersson, S.Tafuri K. Engström, H.Söröd, F. Edelvik, and J.S Carlson. “Simulation of Electrostatic Rotary Bell Spray Paintings in Automotive Paint Shops”. In: Begell House Inc. (2013).

[9] Simon Ingelsten, Andreas Mark, and Fredrik Edelvik. “A Lagrangian-Eulerian framework for simulation of transient viscoelastic fluid flow”. In: Journal of Non-Newtonian Fluid Mechanics 266 (2019), pp. 20–32. ISSN: 0377-0257. DOI: https://doi.org/10.1016/j.jnnfm.2019.02.005. URL: https://www.sciencedirect.com/science/article/pii/S037702571830137X.

[10] Tomas Johnson, Stefan Jakobsson, Benjamin Wettervik, Björn Andersson, Andreas Mark, and Fredrik Edelvik. “A finite volume method for electrostatic three species negative corona discharge simulations with application to externally charged powder bells”. In: Journal of Electrostatics 74 (2015), pp. 27–36. ISSN: 0304-3886. DOI: https://doi.org/10.1016/j.elstat.2014.12.009. URL: https://www.sciencedirect.com/science/article/pii/S0304388614001338.

[11] Tomas Johnson, Andreas Mark, Niklas Sandgren, Lars Erhardsson, Simon Sandgren, and Fredrik Edelvik. “Efficient Simulation of Convective Ovens in Automotive Paintshops”. In: Journal of Heat Transfer 144.9 (June 2022). 094501. ISSN: 0022-1481. DOI: 10.1115/1.4054599. eprint: https://asmedigitalcollection.asme.org/heattransfer/article-pdf/144/9/094501/6886258/ht_144_09_094501.pdf. URL: https://doi.org/10.1115/1.4054599.

[12] Dimitri Nowak, Tomas Johnson, Andreas Mark, Charlotte Ireholm, Fabio Pezzotti, Lars Erhardsson, Daniel Ståhlberg, Fredrik Edelvik, and Karl-Heinz Küfer. “Multicriteria Optimization of an Oven With a Novel -Constraint-Based Sandwiching Method”. In: Journal of Heat Transfer 143.1 (Nov. 2020). 012101. ISSN: 0022-1481. DOI: 10.1115/1.4048737. eprint: https://asmedigitalcollection.asme.org/heattransfer/article-pdf/143/1/012101/6587925/ht_143_01_012101.pdf. URL: https://doi.org/10.1115/1.4048737.

[13] Daniel Gleeson, Stefan Jakobsson, Raad Salman, Fredrik Ekstedt, Niklas Sandgren, Fredrik Edelvik, Johan S. Carlson, and Bengt Lennartson. “Generating Optimized Trajectories for Robotic Spray Painting”. In: IEEE Transactions on Automation Science and Engineering 19.3 (2022), pp. 1380–1391. DOI: 10.1109/TASE.2022.3156803.

[14] Benjamin Wettervik, Tomas Johnson, Stefan Jakobsson, Andreas Mark, and Fredrik Edelvik. “A domain decomposition method for three species modeling of multi-electrode negative corona discharge–With applications to electrostatic precipitators”. In: Journal of Electrostatics 77 (2015), pp. 139–146.

[15] Sebastian Tafuri, Fredrik Ekstedt, Johan S Carlson, Andreas Mark, and Fredrik Edelvik. "Improved spray paint thickness calculation from simulated droplets using density estimation". In: International Design Engineering Technical Conferences and Computers and Information in Engineering Conference. Vol. 45011. American Society of Mechanical Engineers. 2012, pp. 339–347.

[16] Andreas Mark and Berend G.M. van Wachem. "Derivation and validation of a novel implicit second-order accurate immersed boundary method". In: Journal of Computational Physics 227.13 (2008), pp. 6660–6680. ISSN: 0021-9991. DOI: https://doi.org/10.1016/j.jcp.2008.03.031. URL: https://www.sciencedirect.com/science/article/pii/S0021999108001770.

[17] Andreas Mark, Robert Rundqvist, and Fredrik Edelvik. "Comparison between different immersed boundary conditions for simulation of complex fluid flows". In: Fluid dynamics & materials processing 7.3 (2011), pp. 241–258.

[18] Yen-Chi Chen. "A tutorial on kernel density estimation and recent advances". In: Biostatistics & Epidemiology 1.1 (2017), pp. 161–187. DOI: 10.1080/24709360.2017.1396742. eprint: https://doi.org/10.1080/24709360.2017.1396742. URL: https://doi.org/10.1080/24709360.2017.1396742.

[19] A. Bukhvostova, E. Russo, J.G.M. Kuerten, and B.J. Geurts. "Comparison of DNS of compressible and incompressible turbulent droplet-laden heated channel flow with phase transition". In: International Journal of Multiphase Flow 63 (2014), pp. 68–81. ISSN: 0301-9322. DOI: https://doi.org/10.1016/j.ijmultiphaseflow.2014.03.004. URL: https://www.sciencedirect.com/science/article/pii/S0301932214000524.

[20] Laurent Boudin, Laurent Desvillettes, and Renaud Motte. "A modelling of compressible droplets in a fluid". In: International Press 1, No 4 (2003), pp. 657–669.

[21] J Kim and P Moin. "Application of a fractional-step method to incompressible Navier-Stokes equations". In: Journal of Computational Physics 59.2 (1985), pp. 308–323. ISSN: 0021-9991. DOI: https://doi.org/10.1016/0021-9991(85)90148-2. URL: https://www.sciencedirect.com/science/article/pii/0021999185901482.

[22] Dongjoo Kim and Haecheon Choi. "A Second-Order Time-Accurate Finite Volume Method for Unsteady Incompressible Flow on Hybrid Unstructured Grids". In: Journal of Computational Physics 162.2 (2000), pp. 411–428. ISSN: 0021-9991. DOI: https://doi.org/10.1006/jcph.2000.6546. URL: https://www.sciencedirect.com/science/article/pii/S002199910096546X.

A

Tabulated Errors

A.1 Height Sweep No Particles

Table A.1: Tabulated errors from Section 3.1 and Figure 3.3a

	0 cm		1 cm		2 cm		3 cm		4 cm	
	Out	In	Out	In	Out	In	Out	In	Out	In
E	7.8%	17.0%	1.8%	3.4%	0.7%	1.7%	0.3%	1.3%	0.2%	1.1%

Table A.2: Tabulated errors from Section 3.1 and Figure 3.3b

	0.0 cm		0.1 cm		0.2 cm		0.3 cm		0.5 cm		1 cm	
	Out	In	Out	In	Out	In	Out	In	Out	In	Out	In
E	7.8%	17.0%	7.1%	17.3%	4.6%	11.7%	3.7%	9.8%	2.6%	7.0%	1.8%	3.4%

A.2 Height Sweep With Particles

Table A.3: Tabulated errors from Section 3.2 and Figure 3.6a

	0.5 cm		1 cm		2 cm		3 cm		4 cm	
	Out	In	Out	In	Out	In	Out	In	Out	In
E	2.3%	3.7%	2.5%	2.8%	2.4%	2.1%	2.3%	1.7%	2.0%	1.5%

A.3 Cross Validation

Table A.4: Tabulated errors from Section 3.2.1

	DV50				Axial velocity				Slip Factor			
	10 $[\mu m]$		40 $[\mu m]$		10.4 $[m/s]$		17.4 $[m/s]$		0.62 [-]		1.04 [-]	
	Out	In	Out	In	Out	In	Out	In	Out	In	Out	In
E_{inc}	1.3%	2.7%	2.0%	4.7%	2.5%	3.7%	2.2%	3.7%	1.8%	4.0%	2.7%	3.4%
E_{cross}	1.1%	2.9%	0.7%	2.0%	0.32%	0.24%	0.3%	0.2%	0.6%	1.0%	0.7%	1.0%
E_{tot}	1.8%	5.0%	1.9%	3.3%	2.5%	3.8%	2.2%	3.5%	1.7%	3.2%	2.8%	4.1%

B

Cross Validation Flow Fields

The following Appendix illustrates the differences in the flow fields obtained in the cross validation part of the thesis, Section 3.2.1. There will for every injection case described in Section 3.2.1 be three associated images where (a) shows the fully compressible near-bell region, (b) shows the flow field with the incompressible simplification to the height $0.5\,cm$ and (c) shows the flow field after the remaining compressible boundary condition was crossed with the base injection case.

B.1 dv50

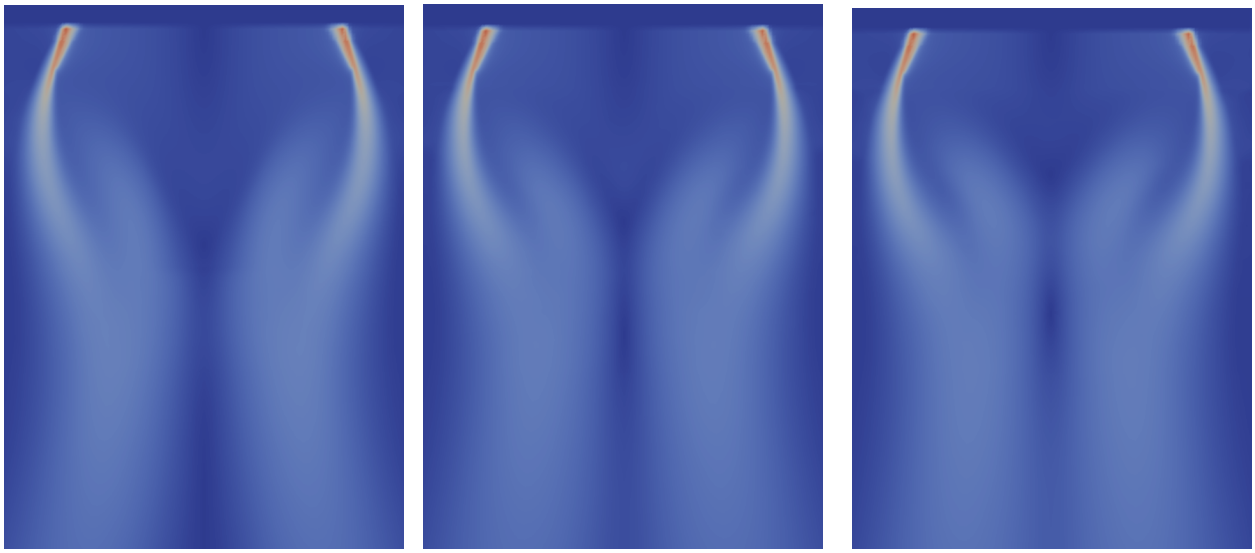

(a) $5\,cm$ **(b)** $0.5\,cm$ **(c)** Cross

Figure B.1: Flow field development for dv50 at $10\,\mu m$

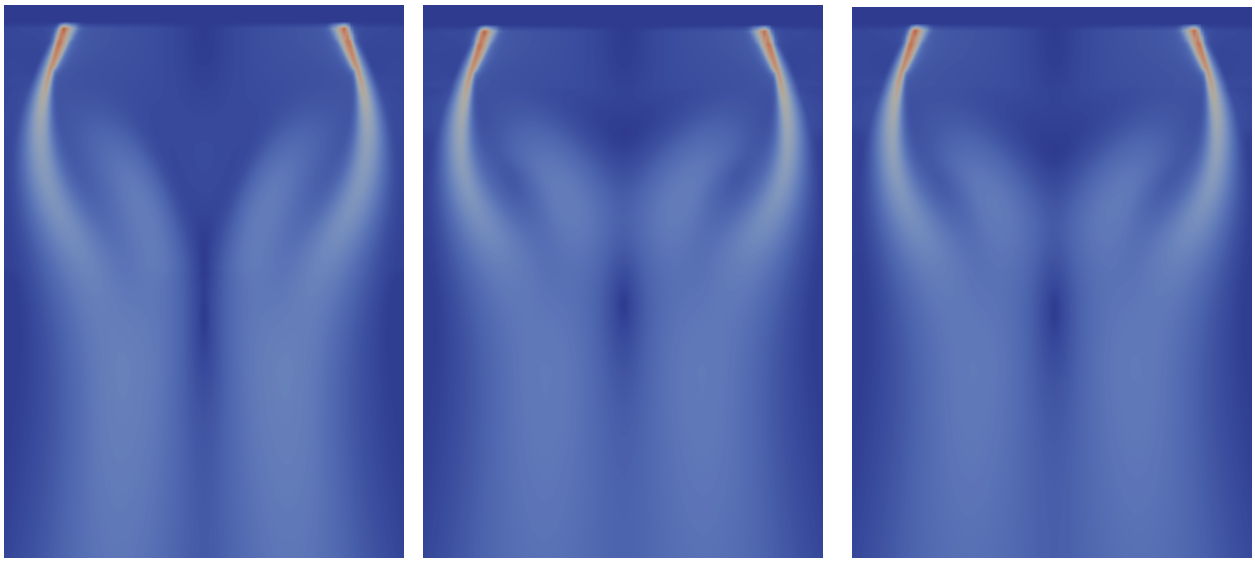

(a) 5 cm **(b)** 0.5 cm **(c)** Cross

Figure B.2: Flow field development for dv50 at 40 μm

B.2 Axial Velocity

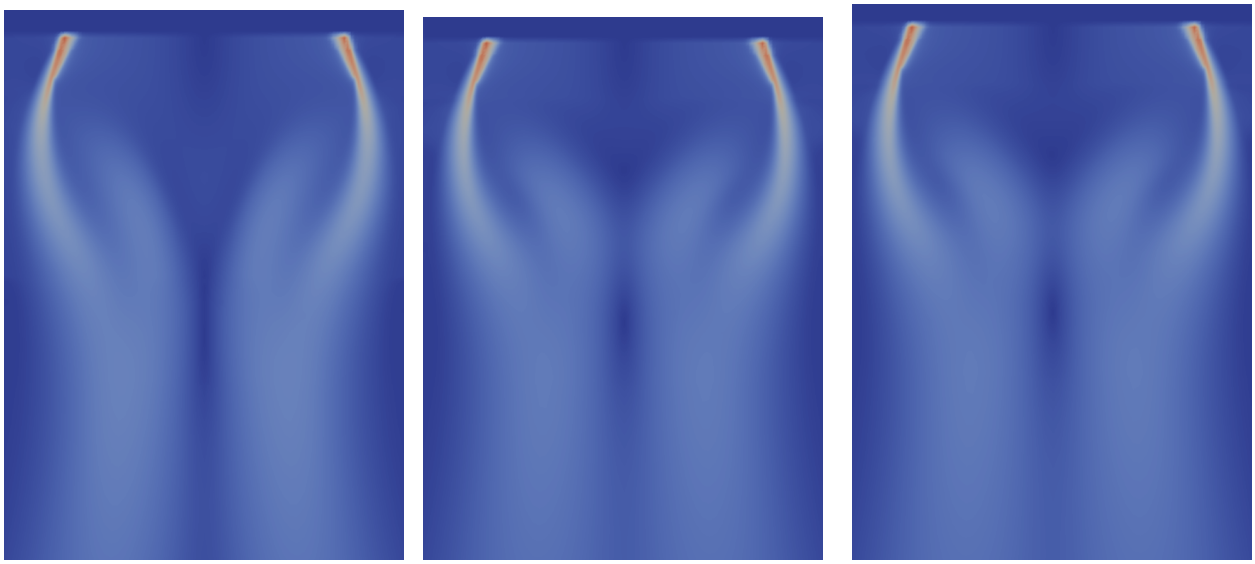

(a) 5 cm **(b)** 0.5 cm **(c)** Cross

Figure B.3: Flow field development for axial velocity at 10.4 m/s

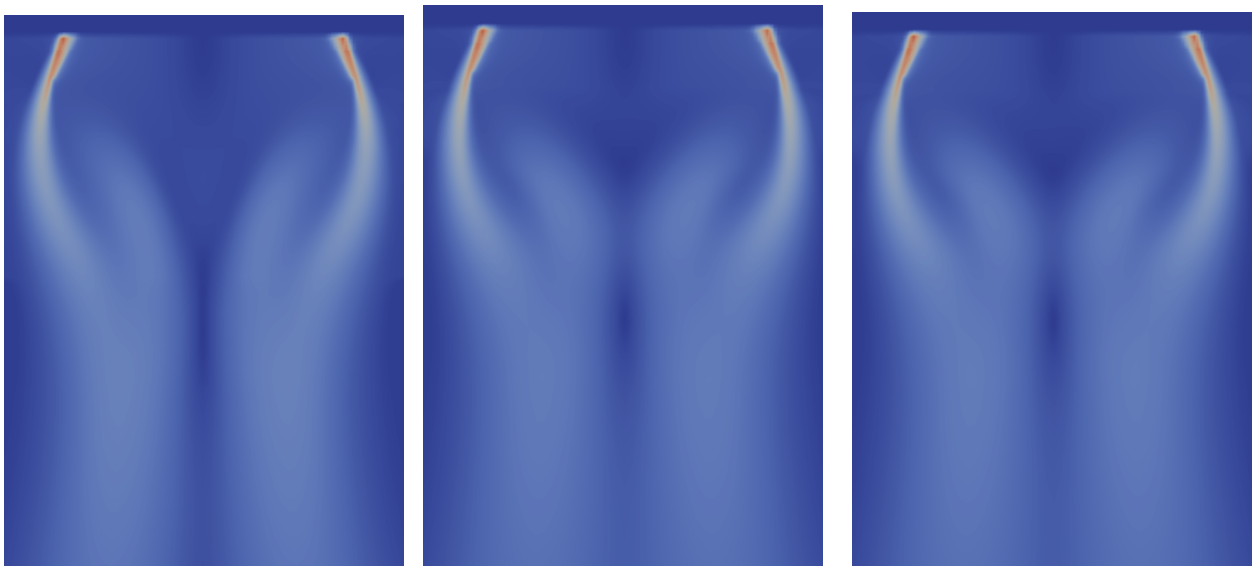

(a) 5 cm **(b)** 0.5 cm **(c)** Cross

Figure B.4: Flow field development for axial velocity at 17.4 m/s

B.3 Slip Factor

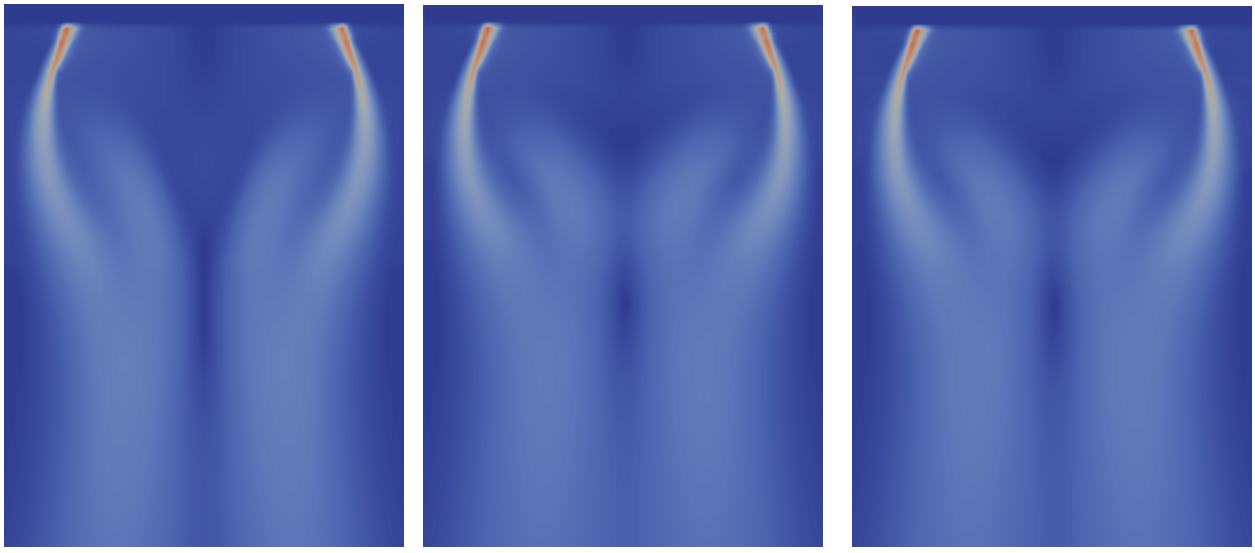

(a) 5 cm **(b)** 0.5 cm **(c)** Cross

Figure B.5: Flow field development for slip factor at 0.62

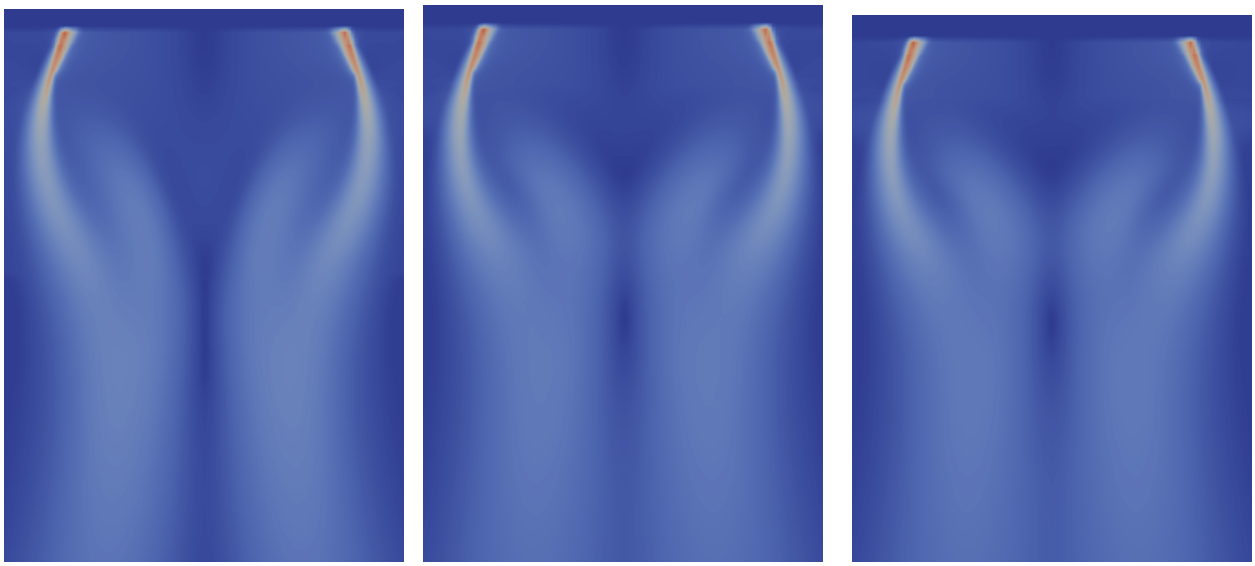

(a) 5 cm **(b)** 0.5 cm **(c)** Cross

Figure B.6: Flow field development for slip factor at 1.04

DEPARTMENT OF MECHANICS AND MARITIME SCIENCES

CHALMERS UNIVERSITY OF TECHNOLOGY
Gothenburg, Sweden 2023
www.chalmers.se

CHALMERS
UNIVERSITY OF TECHNOLOGY